Near Surface Atmospheric Temperatures at Jezero From Mars 2020 MEDA Measurements

A. Munguira[1] , R. Hueso[1] , A. Sánchez-Lavega[1] , M. de la Torre-Juarez[2], G. M. Martínez[3] , C. E. Newman[4] , E. Sebastian[5], A. Lepinette[5], A. Vicente-Retortillo[5] , B. Chide[6] , M. T. Lemmon[7] , T. Bertrand[8] , R. D. Lorenz[9] , D. Banfield[10], J. Gómez-Elvira[5], J. Martín-Soler[5], S. Navarro[5], J. Pla-García[5] , J. A. Rodríguez-Manfredi[5], J. Romeral[5], M. D. Smith[11] , and J. Torres[5]

[1]Física Aplicada, Escuela de Ingeniería de Bilbao, Universidad del País Vasco UPV/EHU, Bilbao, Spain, [2]Jet Propulsion Laboratory, California Institute of Technology, Pasadena, CA, USA, [3]Lunar and Planetary Institute, Houston, TX, USA, [4]Aeolis Research, Chandler, AZ, USA, [5]Centro de Astrobiología (INTA-CSIC), Madrid, Spain, [6]Los Alamos National Laboratory, Los Alamos, NM, USA, [7]Space Science Institute, College Station, TX, USA, [8]LESIA, Observatoire de Paris, Meudon, France, [9]Johns Hopkins Applied Physics Laboratory, Laurel, MD, USA, [10]Cornell Center for Astrophysics and Planetary Science, Cornell University, Ithaca, NY, USA, [11]NASA Goddard Space Flight Center, Greenbelt, MD, USA

Abstract The Mars Environmental Dynamics Analyzer instrument on Mars 2020 has five Atmospheric Temperature Sensors at two altitudes (0.84 and 1.45 m) plus a Thermal InfraRed Sensor that measures temperatures on the surface and at ∼40 m. We analyze the measurements from these sensors to describe the evolution of temperatures in Jezero up to mission sol 400 (solar longitude L_S = 13°–203°). The diurnal thermal cycle is characterized by a daytime convective period and a nocturnal stable atmosphere with a variable thermal inversion. We find a linear relationship between the daytime temperature fluctuations and the vertical thermal gradient with temperature fluctuations that peak at noon with typical values of 2.5 K at 1.45 m. In the late afternoon (∼17:00 Local True Solar Time), the atmosphere becomes vertically isothermal with vanishing fluctuations. We observe very small seasonal changes in air temperatures during the period analyzed. This is related to small changes in solar irradiation and dust opacity. However, we find significant changes in surface temperatures that are related to the variety of thermal inertias of the terrains explored along the traverse of Perseverance. These changes strongly influence the vertical thermal gradient, breaking the nighttime thermal inversion over terrains of high thermal inertia. We explore possible detections of atmospheric tides on near-surface temperatures and we examine variations in temperatures over timescales of a few sols that could be indicative of atmospheric waves affecting near-surface temperatures. We also discuss temperatures during a regional dust storm at L_S = 153°–156° that simultaneously warmed the near surface atmosphere while cooling the surface.

Plain Language Summary The Mars Environmental Dynamics Analyzer instrument on the Mars 2020 Perseverance rover records temperatures in Jezero at four altitudes from the surface to 40 m. We describe the evolution of temperatures over the first 400 Martian days of the mission from northern spring to early autumn. Diurnal temperatures show an unstable convective regime during the daytime and a stable atmosphere at night. Daytime convection produces thermal fluctuations that peak at noon with typical values of 2.5 K at 1.45 m. These thermal fluctuations vanish in the late afternoon when an isothermal atmosphere is observed from the surface up to 40 m. We also find a linear relationship between the daytime temperature fluctuations and the thermal gradient between the surface and the atmosphere. We find very little seasonal change in air temperatures. However, the thermal inertia of the terrain affects surface temperatures, and the nighttime thermal inversion breaks over terrains with high thermal inertia. We investigate the possible detection in near surface temperatures of thermal tides and atmospheric waves. Finally, we show the thermal response of the surface and the atmosphere during the passage of a regional dust storm with a simultaneous cooling of the surface and warming of the near-surface atmosphere.

1. Introduction

The Planetary Boundary Layer (PBL) is the lower part of the atmosphere, where the atmosphere interacts with the surface. On Mars, the PBL typically extends over the first 1–10 km of the atmosphere (Petrosyan et al., 2011; Read et al., 2017). In its lowest part, in the so-called Atmospheric Surface Layer (ASL), thermal and mechanically

driven turbulent processes control the exchange of heat, momentum, and molecular species between the surface and the atmosphere (Stull, 1988). Temperatures play a key role in the dynamics of the ASL, as they largely determine the characteristics of convective activity and the extent of the PBL. This is especially relevant in the tenuous Martian atmosphere, which reacts quickly to changes in irradiation over diurnal and seasonal cycles (Smith et al., 2017).

A variety of orbiters and landed missions have obtained measurements of ground and near-surface air temperatures on Mars (see review in James et al., 2017). However, while orbiters provide greater global spatial coverage and can measure the vertical structure of atmospheric temperatures, the study of thermal processes close to the surface requires in situ measurements.

The Viking Landers VL1 and VL2 provided the first in situ meteorological data from the red planet (Hess et al., 1977; Sutton et al., 1978), showing the large thermal amplitude and repetitiveness of the diurnal temperature cycle and allowing the first detailed studies of the boundary layer of Mars (Tillman et al., 1994). Later missions obtained key data to characterize the thermal behavior of the ASL. For instance, Mars Pathfinder (MPF) observed strong daytime convective activity and nighttime thermal fluctuations caused by mechanical forcing (Larsen et al., 2002; Schofield et al., 1997). Although the Spirit and Opportunity rovers lacked specific meteorological packages, they were equipped with the Miniature Thermal Emission spectrometer (Mini-TES) instrument that allowed the retrieval of vertical thermal profiles within the lowest 2 km of the PBL (Smith et al., 2004). These experiments characterized the daytime super-adiabatic lapse rate and the nighttime thermal inversion that are found on Mars. The temperature fluctuations at different atmospheric levels were characterized along with their upward propagation with measurements on timescales of 30 s (Mason & Smith, 2021; Smith et al., 2004; Spanovich et al., 2006). Additionally, differences in surface and atmospheric temperatures were found between landing sites with homogeneous (Opportunity) and heterogeneous (Spirit) spatial distributions of surface albedo and thermal inertia (Mason & Smith, 2021). Faster measurements enable the study of turbulent processes in the atmosphere. Davy et al. (2010) examined the temperature time series of the Phoenix lander (PHX), obtained at 0.5 Hz and showed a good correlation between the data and Monin-Obukhov Similarity Theory, which is commonly used to statistically describe the thermal turbulence and heat fluxes in the PBL (Read et al., 2017).

More recent missions like Curiosity in Gale crater and Insight in Elysium Planitia have also recorded temperature data near the surface (Banfield et al., 2020; Gómez-Elvira et al., 2012). These missions have measured temperatures over different seasons and dust storms (Ordonez-Etxeberria et al., 2020; Viúdez-Moreiras et al., 2020). However, different thermal contamination effects in these two platforms are difficult to quantify (e.g., Gómez-Elvira et al., 2012), and the details of the seasonal variation of the diurnal cycles of temperatures and thermal fluctuations in the locations of those two missions remain difficult to assess.

The Mars 2020 Perseverance rover has been exploring Jezero crater (18.44°N, 77.45°E) since 18 February 2021. The Mars Environmental Dynamics Analyzer (MEDA) instrument (Rodriguez-Manfredi et al., 2021) on the rover is a set of meteorological sensors that measures several environmental variables, including temperatures at four altitudes from the surface up to ∼40 m. Simultaneous wind data, measured by MEDA at 1.5 m, are important for understanding the temperature measurements, as winds determine whether local heating by the rover and its Radioisotope Thermoelectric Generator (RTG) affects the temperature measurements at specific times of the sol (Gómez-Elvira et al., 2012; Lorenz & Sotzen, 2014). Identifying periods of thermal contamination when winds are available, and observing the behavior of temperatures at those times, allows us to identify similar cases even if winds are not measured. In MEDA, the combination of temperature and wind measurements results in a data set that can overcome many of the limitations of previous surface instruments to study the thermal properties of the ASL.

This paper presents an analysis of the MEDA temperature data up to sol 400 of the mission. This time period extends from northern spring (solar longitude $L_S \sim 13°$, sol 15) to early autumn ($L_S \sim 203°$, sol 400) of Mars Year (MY) 36, in which the rover moved 8.2 km over terrains with different thermophysical properties. The paper is structured as follows: In Section 2, we describe the MEDA sensors, sources of contamination in the raw temperature measurements, and the data used in this investigation. Section 3 shows the resulting decontaminated diurnal cycles of temperatures, their fast fluctuations and thermal gradients. Section 4 focuses on temporal variations of temperatures related to different seasons, surface properties, atmospheric optical depths, and possible effects associated with thermal tides and other atmospheric waves. Section 5 describes the effects on temperatures produced by a regional dust storm that covered Jezero between sols 312 and 318 ($L_S \sim 153°–156°$). A brief
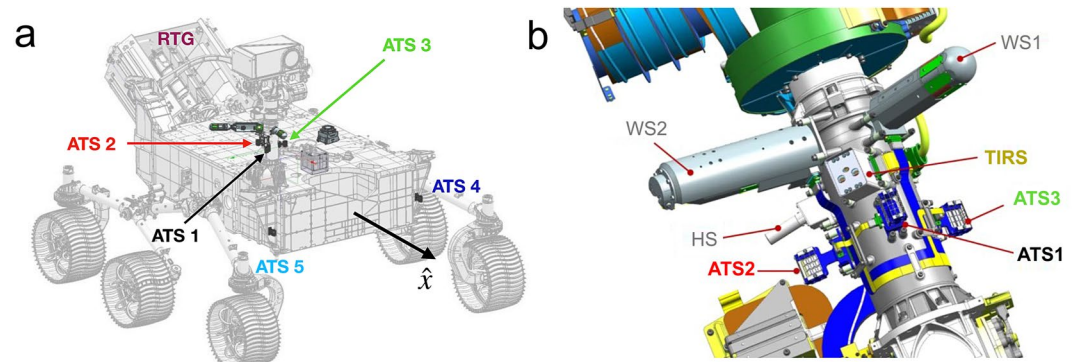
Figure 1. (a) Location of the five Air Temperature Sensors (ATS) and the Radioisotope Thermoelectric Generator. The color code for each ATS will be preserved through the different figures showing ATS data. The Rover Arm (not shown) is located on the front left of the rover, partially covering ATS4. (b) Detailed distribution on the Remote Sensing Mast of ATS1, ATS2, ATS3 as well as the two Wind Sensors booms, TIRS and the Humidity Sensor (HS). Adapted from Rodriguez-Manfredi et al. (2017) and Rodriguez-Manfredi et al. (2021). ATS4 and ATS5 appear mislabeled in Rodríguez-Manfredi et al. (2021) whereas this figure shows the correct location of both sensors.

comparison of the MEDA thermal data with temperatures observed by other missions and predicted by models is carried out in Section 6. The conclusions are summarized in Section 7. Two Appendices discuss technical aspects of the thermal contamination sources (Appendix A) and a selection algorithm to obtain environmental temperatures from raw Air Temperature Sensors (ATS) data (Appendix B). Martian Local True Solar Time (LTST) is used to discuss times throughout this paper.

2. Data Description and Sensor Characteristics

The MEDA instrument (Rodriguez-Manfredi et al., 2021) measures environmental variables around the clock in sessions that can be as short as 5 min or as long as several hours to adapt to mission requirements. Typically, MEDA covers over 55% of each sol following a measurement pattern, planned using Local Mean Solar Time, that covers even hours in even-numbered sols and odd hours in odd-numbered sols (see Figure S1 in Supporting Information S1). Thus, in most cases, the combination of data from two consecutive sols allows us to fill in complete diurnal cycles. The full data set allows us to study timescales ranging from those associated with atmospheric turbulence to diurnal cycles and their seasonal evolution. The MEDA data sets that are involved in the analysis of temperatures are provided by the ATS, the Thermal Infrared Sensor (TIRS), and the Wind Sensors (WS). Both ATS and WS can record data with a frequency up to 2 Hz, whereas TIRS is limited to a frequency of 1 Hz.

2.1. ATS

MEDA has five ATS located at two altitudes: two sensors at 0.84 m on the front of the rover (ATS4 and ATS5) and three sensors at 1.45 m (ATS1-3) around the Remote Sensing Mast (RSM). The latter are azimuthally distributed so that at least one sensor is always located upwind of the RSM (Figure 1). This configuration ensures that, under most conditions, the air arriving to at least one of the three sensors is not thermally contaminated by the presence of the rover (Rodriguez-Manfredi et al., 2021). However, the two sensors at 0.84 m are partially shielded from the environment, and their measurements are subject to higher levels of thermal contamination.

The MEDA ATS sensors are based on thin-wire thermocouples and were designed to have a response time faster than 1 s under all Martian conditions (Perez-Grande et al., 2017; Rodriguez-Manfredi et al., 2021). This requirement was tested in calibration experiments and was confirmed after landing on Mars with real data, for example, rapid temperature increases are observed coinciding with close passages of vortex cores (Hueso et al., 2023; Newman et al., 2022). The ATS data accuracy is better than ± 1 K, with a resolution including noise better than 0.1 K (Rodriguez-Manfredi et al., 2021). Compared to other missions, the lower thermal inertia of MEDA's ATS enables faster response times and more precise data. For instance, VL1 and VL2 had narrow thermocouple sensors at a single altitude (Hess et al., 1977), MPF had a mast with thermocouple sensors at three elevations above the surface (Schofield et al., 1997), and PHX had thermocouples at three altitudes above the

lander deck (Davy et al., 2010). All these missions used thermocouples with 50–70 micron wires that responded within seconds to atmospheric temperature changes. The Curiosity rover (MSL) (Gómez-Elvira et al., 2012) and InSight lander (Banfield et al., 2019) used platinum resistance thermistors with longer response times, measuring low-pass-filtered versions of the atmospheric temperature.

The ATS measure the local air temperature around the sensors, which are embedded in the rover's thermal boundary layer. This is especially relevant at sunrise/sunset, when the air surrounding the rover warms/cools at a different rate compared to the atmosphere and the surface. Computational Fluid Dynamics (CFD) simulations based on the methodology presented by Bardera et al. (2018) show that background winds as low as 2 m/s are sufficient to couple the ATS1-3 sensors upwind of the RSM to the atmosphere (Figure S2 in Supporting Information S1), allowing for precise measurements of environmental temperatures. Comparisons of simultaneous ATS1-3 and wind data suggest that even smaller winds are able to couple the sensors to the atmosphere (Appendix A). ATS4 and ATS5 are also decoupled from the rover's thermal boundary layer when winds come from the frontal and lateral side of each sensor. However, ATS4, which is located behind Perseverance's warm 7-foot-long Robotic Arm (not shown in Figure 1a), is less exposed to environmental winds and typically records a higher temperature than ATS5.

A comparative analysis of ATS measurements with wind data and the rover's orientation (Appendix A) reveals that, in most cases, the minimum temperature of the three ATS at the RSM can be considered a reliable measure of the environmental temperature. The minimum of ATS4 and ATS5 might still have some thermal contamination because winds from a wide range of directions cannot completely decouple these sensors from the thermal boundary layer of the rover. In order to preserve the thermal fluctuations in the data, we use an algorithm that analyzes the signals from the five ATS and produces temperatures at 0.84 and 1.45 m, following the lower temperature at each altitude and sliding gradually from one sensor to another while preserving temperature fluctuations (Appendix B).

Finally, thermal perturbations from the RTG can affect the ATS measurements on the RSM when winds of $\sim$2–4 ms^{-1} blow from the back of the rover (Gómez-Elvira et al., 2012; Lorenz & Sotzen, 2014). The two sensors at 0.84 m on the front of the rover are shielded from RTG effects and serve to identify episodes of RTG contamination. Several observations of RTG contamination events combined with simultaneous wind data show that these are typically short duration events that occur mostly during the night and do not have an overall impact in the measurements of the daily cycle of temperatures (Appendix A and Figure S3 in Supporting Information S1). Note that the RTG effects cannot be filtered out completely when they affect the measurements of the three ATS at the mast, but in this case the algorithm will select the ATS downwind from the RSM (typically ATS1) that records the lowest amplitude of the thermal plume.

2.2. TIRS and WS

TIRS is a thermal infrared radiometer that among other measurements retrieves the ground brightness temperature from the upward infrared flux and the atmospheric temperature within the lower PBL from the downwelling infrared flux at the 15 μm CO_2 emission band. This downwelling flux is sensitive to temperatures from a layer with an effective thickness of $\sim$200 m and has a peak contribution from the air at an altitude of $\sim$40 m, which is the effective atmospheric level in the retrieval of TIRS air temperatures (Rodriguez-Manfredi et al., 2021). Together with the two levels studied with ATS, TIRS allows us to evaluate the vertical thermal gradient and its evolution in the Martian ASL. Temperature measurements from TIRS reach an accuracy of 0.75 and 2.83 K for the ground and air temperatures respectively, with nominal noise levels of 0.08 and 0.45 K (Rodriguez-Manfredi et al., 2021; Sebastián et al., 2021). The upward looking channel is strongly perturbed by the solar radiation when the sun enters its Field of View (FoV). This circumstance is labeled with the corresponding flag in the TIRS data files allowing such data to be filtered-out from the analysis.

The TIRS ground temperature channel has a FoV that covers an ellipse of about 3 m^2 pointed $\sim$3.75 m away from the RTG to minimize thermal contamination (Pérez-Izquierdo et al., 2018). The ground temperature is measured integrating the upward long-wave infrared flux from 8 to 14 μm (Sebastián et al., 2020). Because surface emissivities can vary from site to site and are unknown, they are not accounted for in the instrument calibration and, as a result, retrieved ground brightness temperatures can be slightly lower than actual kinetic temperatures (Sebastián et al., 2020, 2021). Based on past experience with similar sensors on MSL, the largest uncertainties in ground

temperatures coming from surface properties are estimated to be ∼3 K in the early morning and ∼5 K near noon (Hamilton et al., 2014).

Winds are recorded by the WS with two booms that are azimuthally separated by 120° to enable accurate wind retrievals regardless of wind direction. This is necessary because both booms are attached to the rover's RSM, which perturbs winds approaching from the rear of each boom (Rodriguez-Manfredi et al., 2021). Each boom contains six thermal anemometers in which a cold die and four hot dice are exposed to the environment, and the electrical current required to keep the hot dice temperature constant is measured. The wind data retrieval is based on calibration activities in a wind tunnel. A boom selection algorithm chooses which of the two booms provides the closest to the true environmental winds at any moment; these selections are available in the NASA Planetary Data System (PDS) data set within the derived data products (DER files).

Specific analysis of TIRS and WS data beyond their relationship with temperatures are presented by Martínez et al. (2023), Vicente-Retortillo et al. (2022), Newman et al. (2022) and Viúdez-Moreiras, Lemmon, et al. (2022), Viúdez-Moreiras, de la Torre-Juarez, et al. (2022).

3. Diurnal Cycles of Temperatures and Temperature Fluctuations

Appendix B describes the process to get a single environmental temperature measurement at 1.45 m from local air temperatures recorded by ATS1-3 at the RSM. It also describes the reduction of air temperatures recorded by ATS4-5 into a single temperature at 0.84 m. These ATS derived temperatures, as well as the programs required to calculate them, are provided for the sols studied in this manuscript in Hueso et al. (2022). Hereinafter, we study actual environmental temperatures extracted from ATS and TIRS data.
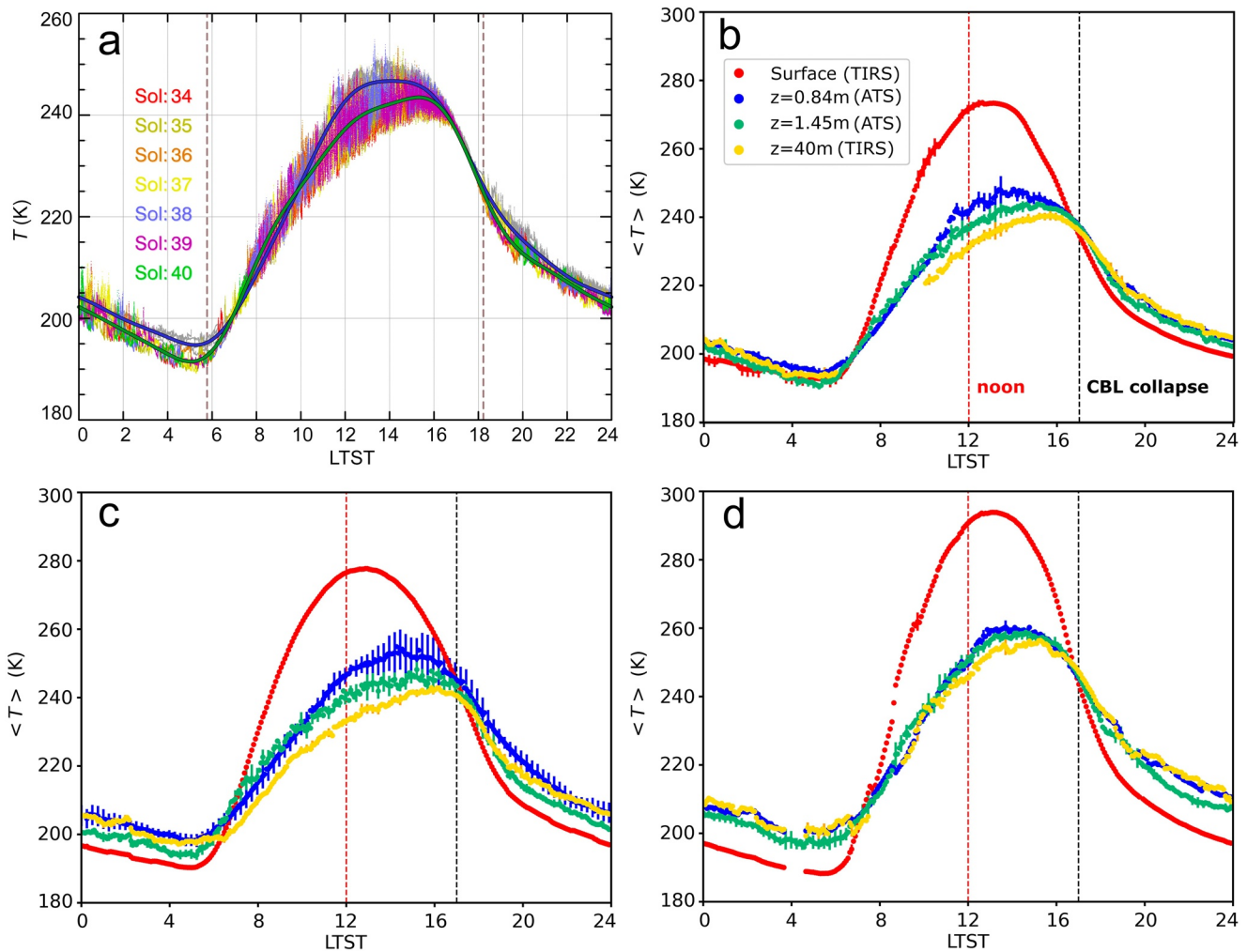
3.1. Diurnal Cycle of Temperatures

Complete diurnal temperature cycles at four altitudes (surface, 0.84 m, 1.45 m, and 40 m) can be obtained by combining ATS and TIRS data from consecutive sols that share similar conditions, for example, the same rover orientation and similar surface properties. Representative examples at different L_S are given in Figure 2.

Derived ATS temperatures at 0.84 and 1.45 m between sols 34 and 40 ($L_S \sim 25°$) are shown in Figure 2a. This figure shows that the diurnal temperature cycles change very little in consecutive sols. Figures 2b–2d show diurnal temperature cycles based on averages over time windows of 5 min at the surface, 0.84, 1.45, and 40 m and at L_S values of 25°, 90°, and 180°, extending beyond results presented in Rodríguez-Manfredi et al. (2023). The greater variability found in the comparison of these plots is observed in surface temperatures, and is driven by a combination of seasonal changes and differences in local thermophysical properties of the explored terrains. Table 1 highlights in a numeric form the characteristic temperatures of each period in Figures 2b–2d.

Vertical thermal profiles can be obtained at different times. Figure 3 shows an example of the diurnal evolution of the vertical thermal profile for sols 186–194 ($L_S = 92–96°$). This figure ignores the data at 0.84 m due to the lower reliability of ATS4-5 at night. During daytime hours, the solar irradiation heats the surface and part of this heat is transferred as sensible heat to the atmosphere, leading to convective instability and the growth of a Convective Boundary Layer (CBL) (Martínez et al., 2009; Read et al., 2017). This process is accompanied by strong temperature fluctuations, discussed in Section 3.2. The largest temperature difference between the surface and the air at 40 m occurs typically between 11:00 and 12:30 LTST and is ∼43 K at $L_S \sim 90°$ (Figure 3), but this temperature difference can vary for different values of L_S (see Figure 2).

Note that in Figure 2 and Table 1, there is a phase difference between the times when the maximum temperatures are observed at different altitudes. This phase difference changes slightly for different values of L_S. For the L_S period covered in this study, surface temperatures peak slightly after midday (12:30–13:30 LTST), whereas air temperatures at 0.84, 1.45, and 40 m peak at 13:30–15:00, 14:30–15:30, and 15:00–16:30, respectively. These phase changes in the times of the daily maximum temperatures at different levels are a consequence of the atmosphere being heated primarily from below, with nearly constant heat fluxes at all heights within the ASL (Foken, 2008; Martínez et al., 2009; Read et al., 2017).

The daytime convective regime transitions into a calmer period at night with lower temperature fluctuations and the development of a thermal inversion, with typical differences between the surface and air at 40 m of −9 K (Figure 3). From midnight to ∼06:00 LTST, surface and atmospheric temperatures diminish at different cooling

Figure 2. Diurnal cycles of temperature. (a) Air Temperature Sensors (ATS) temperatures for sols 34–40 ($L_S \sim 25°$) at 1.45 m (one color for each sol) and 0.84 m (gray for all sols). The green and blue lines are fits to the combined data at 1.45 and 0.84 m, respectively. Vertical dashed lines mark sunrise and sunset. (b) Averaged temperatures from the surface to 40 m using 5-min time windows over TIRS and ATS data combining sols 34–40. Colors are as indicated in the legend of the figure. Error bars represent standard deviations when averaging temperature values at the same Local True Solar Time (LTST) from multiple sols and are shown every 15 min. Vertical red and black lines indicate noon and the collapse of the Convective Boundary Layer (typically around 17:00 LTST), respectively. (c) Same as (b) but for sols 186–194 ($L_S \sim 90°$). (d) Same as (b) but for sols 358–359 ($L_S \sim 180°$). In (d), error bars are only computed in the few 5-min time windows in which data for both sols are available. Gaps in TIRS data in (b, d) are due to either calibration activities or direct sunlight entering the Field of View of TIRS air temperature channel.

rates, and the thermal inversion tends to weaken progressively, although gradually. The apparent variability of the nighttime thermal inversions observed over terrains with different thermal inertia is discussed in Section 4.

Each sol, there are two transition periods between the daytime convective period and the nighttime stable period. The first transition is after sunrise, when the thermal inversion vanishes quickly as the surface and atmospheric temperatures increase. The second transition is in the afternoon, at around 16:30-17:30 LTST, depending on season, when the thermal fluctuations vanish progressively and the crossover of surface and atmospheric temperatures results in the CBL collapse. Figure 3 shows in black the vertical thermal profile from 17:00 to 17:30 LTST. This is a detection of a nearly isothermal atmosphere from the surface to 40 m that coincides with the vanishing of the temperature fluctuations, similar to previous findings from two heights with the Rover Environmental Monitoring Station (REMS) instrument on MSL (Guzewich et al., 2021).

3.2. Temperature Fluctuations

Air temperatures at 0.84, 1.45, and 40 m show thermal fluctuations on timescales of a few seconds that follow a repeatable diurnal cycle. These fluctuations are stronger during daytime due to convective instability

Table 1
Main Characteristics of the Temperature Diurnal Cycles in Figures 2b–2d Using Data From Consecutive Sols

| L_S (°)	Height (m)	T_{mean} (K)	T_{max} (K)	T_{min} (K)	ΔT (K)	LT_{Tmin} (hh:mm)	Sunrise (hh:mm)	LT_{Tmax} (hh:mm)	Sunset (hh:mm)
25	Surface	224	273	192	81	05:30	05:46	12:30	18:14
	0.84	218	247	195	52	05:00	–	14:00	–
	1.45	216	243	191	52	05:00	–	15:00	–
	40	215	240	194	46	05:00	–	15:30	–
90	Surface	227	277	191	86	05:00	05:40	12:30	18:37
	0.84	223	253	198	55	05:00	–	14:30	–
	1.45	219	247	194	53	05:00	–	15:00	–
	40	218	243	197	46	05:00	–	16:00	–
180	Surface	230	293	189	104	05:30	06:00	13:00	18:00
	0.84	226	260	200	60	05:00	–	13:30	–
	1.45	224	258	197	61	05:00	–	14:30	–
	40	226	256	201	55	05:00	–	15:00	–

Note. The times for maximum and minimum temperatures are given in windows with a resolution of 30 min (starting at the times shown in the table). ΔT is the amplitude of the diurnal thermal cycle calculated as $\Delta T = T_{max} - T_{min}$.

(Davy et al., 2010). To examine temperature fluctuations, we fit and extract a second-order polynomial to the temperature time series in time windows of 5 min. This removes the effects of the diurnal evolution and thermal effects of any atmospheric structure with periods longer than ~10 min. We then measure the standard deviation, σ_T, of the remaining high-frequency temperature fluctuations.

The strongest temperature fluctuations are observed at 1.45 m. Figure 4a displays values of σ_T at this level for the first 400 sols of the mission. The rover orientation, that is, Perseverance's yaw angle, is colorized to highlight the impact of specific orientations on the derived ATS measurements. In sols that Perseverance is oriented to the West, we observe high temperature fluctuations at 16:30 LTST, when fluctuations typically vanish coinciding with the CBL collapse. This is caused by environmental winds at that time of the day blowing across the rover and injecting thermal perturbations from the rover to the air sampled by the ATS at 1.45 m. Nighttime values of σ_T in Figure 4a are also enhanced by thermal perturbations from the RTG (see Figure S3 in Supporting Information S1) and are apparent at 20hr, 23hr, 01hr and 02hr in Figure 4a. At night, the wind primarily blows from the N/NW/W (Newman et al., 2022; Viúdez-Moreiras, Lemmon, et al., 2022) (this varies with time of sol and from sol to sol). Hence the nighttime RTG-induced perturbations are most evident when the rover heading is to the S/SE/E, except between 01 and 05 LTST when winds are weak with very variable directions. Excluding those events, temperature fluctuations observed by MEDA at 1.45 m are comparable but smaller than those derived
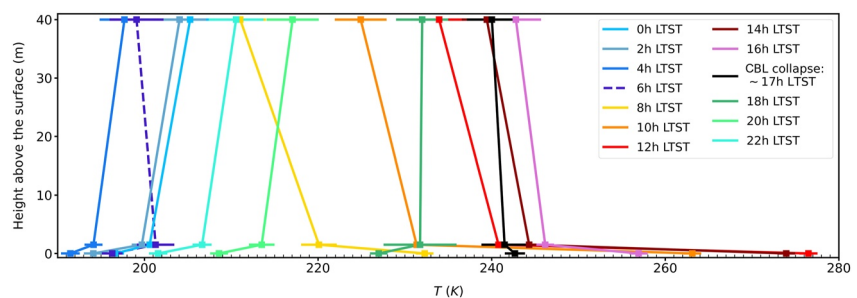
Figure 3. Mean vertical thermal profiles at different Local True Solar Time in time windows of 30 min starting at the times shown in the legend. These profiles have been averaged for sols 186–194 ($L_S = 92$–96°). Squares represent measurements of temperatures at 0, 1.45, and 40 m. Error bars have been calculated as $\sqrt{c^2 + \sigma^2}$, where c is the accuracy of each measurement, discussed in Section 2, and σ is the standard deviation when averaging over sols 186 to 194.
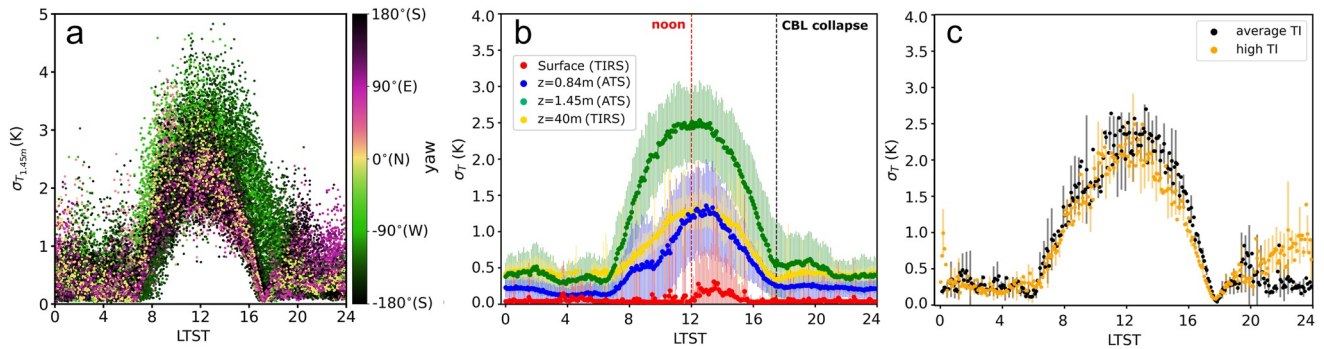
Figure 4. Global pattern of the diurnal temperature fluctuations, σ_T, on Mars Environmental Dynamics Analyzer data in 5-min windows for the first 400 mission sols. (a) Temperature fluctuations from Air Temperature Sensors data at 1.45 m as a function of Local True Solar Time (LTST) and the orientation of the rover. (b) Temperature fluctuations from the surface to 40 m as a function of LTST averaged over 400 sols. (c) Averaged temperature fluctuations at 1.45 m at two sites along the rover trajectory: sols 141–149 (high thermal inertia terrain, orange-yellow dots) and 158–166 (average thermal inertia terrain, black dots). In both (b and c), symbols represent the mean σ_T values at each LTST and error bars show their standard deviation.

from sonic temperatures using the SuperCam Microphone during Laser Induced Breakdown Spectroscopy experiments (Maurice et al., 2021), which sample the atmosphere at an effective height of 0.77 m, and at a faster rate than MEDA (Chide et al., 2022; Maurice et al., 2022).

Figure 4b shows the diurnal evolution of σ_T at the four altitudes sensed by MEDA as a function of LTST averaged over the 400 sols studied. Nighttime RTG effects visible in panel a of this figure largely vanish in panel b because these episodes of thermal contamination are relatively uncommon, and vanish when averaging the σ_T values over several sols. Temperature fluctuations are large during daytime hours and peak at noon due to the convective instability. The highest temperature fluctuations appear to occur at 1.45 m but note that, as described above, the ATS at 0.84 m are largely sheltered from the environmental winds and may not capture the full intensity of thermal fluctuations. Temperature fluctuations at ∼40 m captured by TIRS are smaller at noon than those observed at 1.45 m, in agreement with Mason and Smith (2021), with this reduction of turbulence with height likely caused by mixing as air parcels ascend. At night, temperature fluctuations are also present in the data. Typical values of nighttime fluctuations are below 0.5 K. Both TIRS at 40 m and ATS at 1.45 m result in similar values of the nighttime temperature fluctuations, which are possibly related to changing winds and nighttime shear-driven turbulence.

Seasonal patterns of temperature fluctuations are not evident in the MEDA data so far. However, the magnitude of the temperature fluctuations varies significantly from sol to sol, as shown by the error bars in Figure 4b. This variation might be due to changes in surface properties (Miller et al., 2018), the passage of clouds and dust structures (Chide et al., 2022; Smith et al., 2006) or artificially produced by the rover's thermal boundary layer depending on the orientation of the rover (Appendix A). Figure 4c explores the former case by showing diurnal fluctuations over different terrains, selecting two ranges of sols when Perseverance was parked at two different locations with values of thermal inertia (TI) that are high (sols 141–149, TI = 526 ± 8 J · m^{-2} · K^{-1} · s$^{-1/2}$) and average (sols 158–166, TI = 372 ± 8 J · m^{-2} · K^{-1} · s$^{-1/2}$). To avoid artificial effects, the rover was oriented eastward at both locations. Terrains with a high thermal inertia warm less at noon and result in weaker local thermal gradients at daytime. However, there are no obvious differences in the maximum amplitude of temperature fluctuations at the two sites related to the different thermal gradients (see Section 3.3), suggesting that temperature fluctuations are caused by the horizontal advection of convective eddies over the terrain rather than being related to the local properties of the small terrain patch where TIRS measures the thermal inertia. Nevertheless, the error bars arising in Figure 4c from the averages of eight sols indicate that there are some sol-to-sol variations.

Temperature variations can also be observed in the surface temperature associated with the passage of dusty structures and convective vortices, as described in Hueso et al. (2023), Newman et al. (2022), and Vicente-Retortillo et al. (2022).

3.3. Relationship Between Temperature Fluctuations and the Near-Surface Thermal Gradient

Figure 5 shows an example of the diurnal evolution of temperature fluctuations at 1.45 and 40 m, compared with the vertical thermal gradient. The example corresponds to sols 186 and 187 ($L_S \sim 90°$). At both levels, the
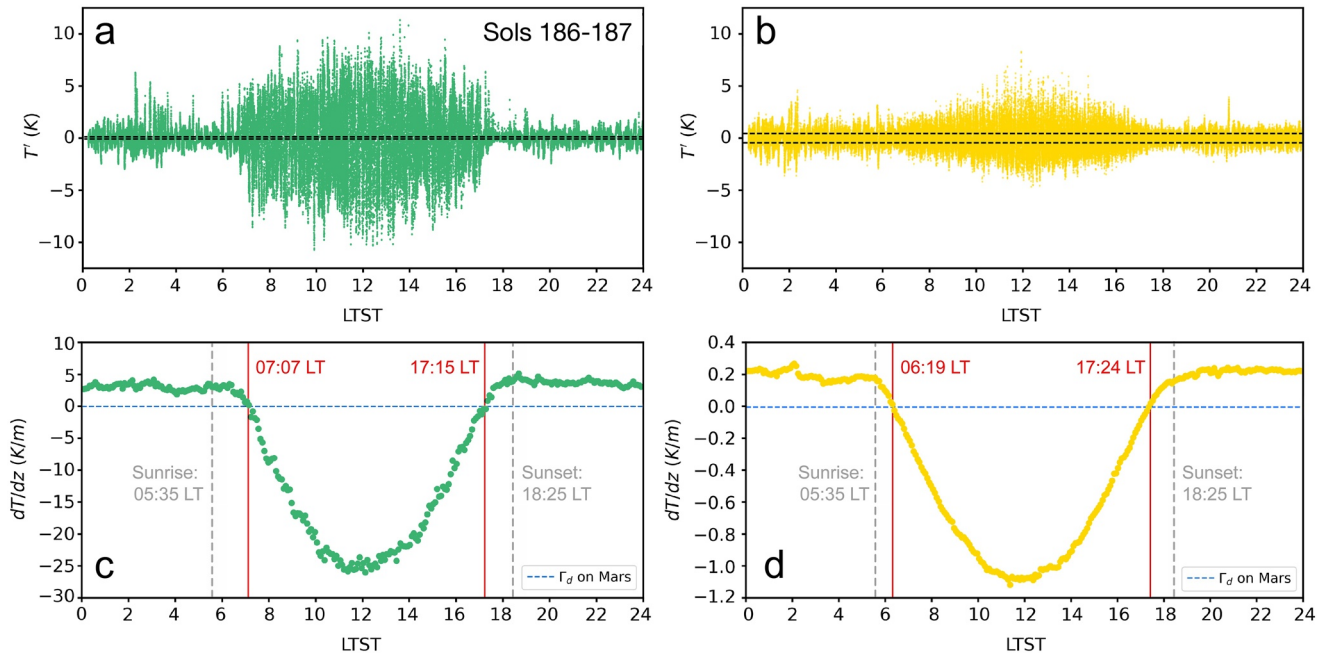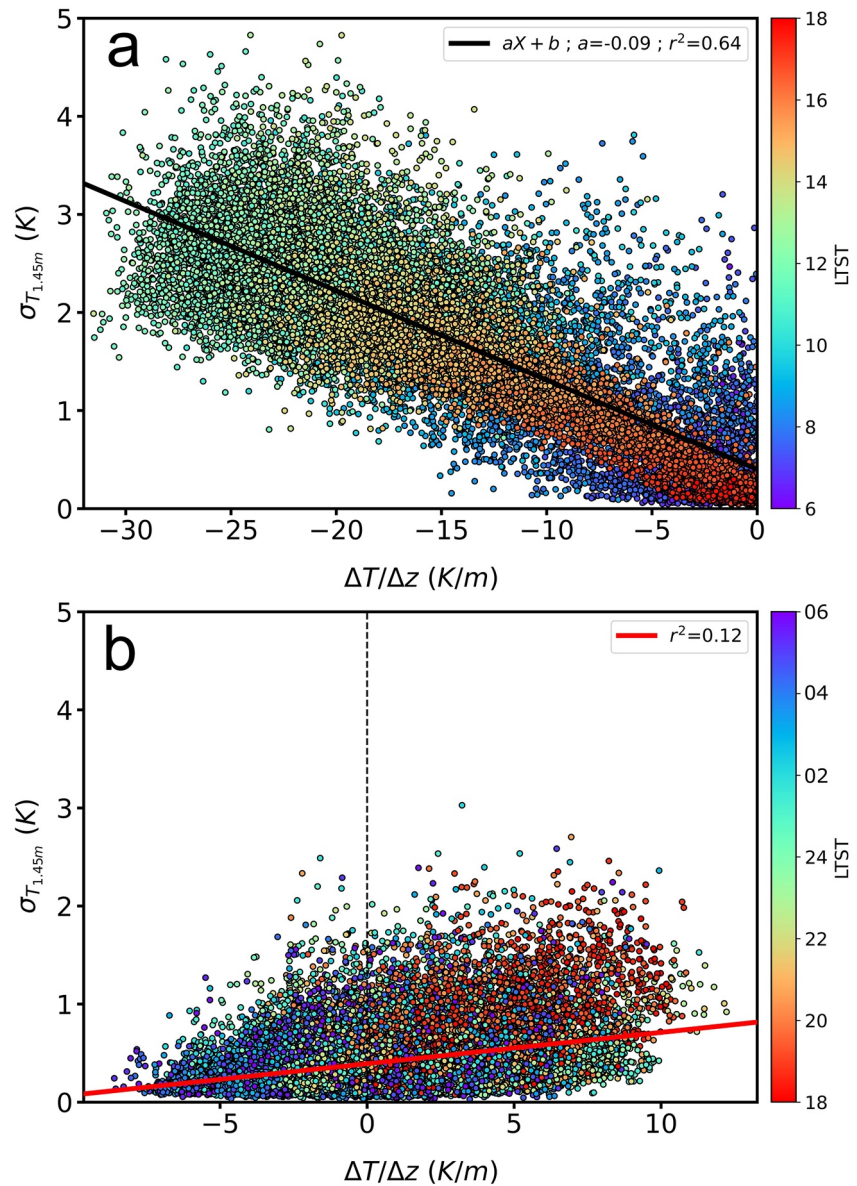
Figure 5. Temperature fluctuations, T', at 1.45 m (a) and 40 m (b), on sols 186 and 187 ($L_S \sim 90°$). Values were calculated after removing a second order polynomial fit to temperatures in windows of 30 min. Horizontal dashed lines show the nominal noise levels of $\sim$0.1 and 0.45 K for the temperatures at 1.45 and 40 m, respectively. (c) 5-min averaged gradients between the surface and 1.45 m and (d) between the surface and 40 m on sols 186–194. The dry adiabatic lapse rate of the Martian atmosphere (-4.5 K km^{-1}) is drawn as a dashed blue line. Note the change in the gradient scale between (c and d). Vertical gray lines in (c and d) mark the sunrise and sunset and vertical red lines show the times when the surface temperature matches that of each layer of the atmosphere.

fluctuations peak near noon, following the trend of the thermal gradient between the surface and the atmosphere, largely diminish and even vanish for stable conditions (Figures 5a and 5b). The maximum amplitudes of the fluctuations are $\sim$11 K at 1.45 m and $\sim$8 K at 40 m. We note, however, that the 95th percentiles between 10:00 and 14:00 LTST are $\sim$6.5 and 3.0 K, for these levels, respectively. At night, strong intermittent fluctuations appear in ATS data when winds carry heat plumes from the RTG toward Perseverance's RSM (examples are the pulses of fluctuations visible in Figure 5a and most noticeable at 2:00 LTST, with more examples in Figure S3 in Supporting Information S1). However, these RTG effects have a small statistical effect, and nighttime fluctuations at 1.45 m are constrained to 1.5 K when considering 95th percentiles of the fluctuations. This value is equivalent to the one found when also examining the 95th percentile of temperature fluctuations at 40 m.

Figures 5c and 5d show the 5-min averaged lapse rates, $\Delta T/\Delta z$, between the surface and 1.45 m and between the surface and 40 m, respectively. The data shown here correspond to sols 186 through 194, a period during which the rover did not move and the daily pattern of temperatures was highly repeatable from sol to sol. The dry adiabatic lapse-rate of the Martian atmosphere is $dT/dz = -g/C_p = -4.5 \times 10^{-3}$ K/m, where g is the acceleration of gravity and C_p is the specific heat at constant pressure of the atmosphere. Thus, a strong super-adiabatic vertical thermal gradient develops during the daytime near the surface from 07:00 to around 17:30 LTST. This thermal gradient concentrates in the first 1.45 m closest to the surface with a maximum lapse rate for these sols of -26 K/m close to 12:00 LTST, following the diurnal insolation cycle. In contrast, a weak thermal inversion is observed at night with a maximum lapse rate of 5 K/m.

Figure 5 indicates that there is a strong correlation between the magnitude of the temperature fluctuations and the vertical thermal gradient. In order to explore this correlation in greater detail, for the first 400 sols of the mission, we show in Figure 6 the temperature fluctuations at 1.45 m, from the standard deviations of temperatures in 5-min windows (σ_T), compared to the corresponding mean thermal gradients between the surface and 1.45 m ($\Delta T/\Delta z$). Panel a in this figure focuses on the daytime hours when a good correlation of both variables is found. The daytime linear relation between temperature fluctuations and the thermal gradient has a coefficient of determination $r^2 = 0.64$ (i.e., 64% of the variance in the data is associated with the linear trend, and residuals from the linear trend are homogeneous and unbiased). Panel b shows the corresponding analysis for the nighttime, in which no

Figure 6. Scatter plots showing the relationship between temperature fluctuations (σ_T) at 1.45 m and the vertical thermal gradients ($\Delta T/\Delta z$). (a) During daytime hours. (b) During nighttime hours. In order to reduce the impact of the rover's thermal boundary layer on the measured temperature fluctuations near sunrise and sunset, between 06:00–10:00 and 14:00–18:00 Local True Solar Time, we filter out data corresponding to rover orientations to the north ($-90° < yaw < 90°$) and to the west ($yaw < 0°$), respectively. The dashed line in (b) delimits the different vertical stability regimes at nighttime (measurements that appear to the left are typically acquired over high thermal inertia terrains). Thick lines show linear fits to the data with a good correlation between both variables during daytime hours ($r^2 = 0.64$) and no correlation during nighttime ($r^2 = 0.12$).

correlation between temperature fluctuations and the atmospheric stability is apparent. This is a consequence of the nighttime temperature fluctuations not being driven by the sensible heat flux, which is negligible at night compared with the radiative fluxes (Martínez et al., 2023).

The empirical relation between the intensity of daytime temperature fluctuations and the vertical thermal gradient from Figure 6a is related to the specific characteristics of the convective turbulence in the ASL at Jezero. The linear relation shown in Figure 6a might serve as an empirical closure parameterization of turbulence in models of the Martian atmospheric circulation. MEDA's simultaneous data on pressure, horizontal winds, temperatures at different levels and vertical stability offer excellent perspectives toward the study of turbulence and thermal fluxes in the Martian ASL that will be explored in the future.

4. Temporal Variations of Atmospheric and Surface Temperatures

Over 400 sols, there are variations in temperatures related to seasonal changes in solar irradiance, varying atmospheric dust opacity, effects associated with the surface properties over the different terrains traversed by Perseverance, and possible atmospheric waves. The combination of these factors makes it difficult to characterize their individual effects on temperatures. Here, we examine the temporal evolution of temperatures from the surface to 40 m.

4.1. Temporal Evolution of Daily Temperatures

We first examine diurnal ATS and TIRS temperature data. To calculate averages over 24 hr, we combine data from two consecutive sols, which together usually cover the entire LTST range (see Section 2). Then, we compute Fourier fits for the diurnal cycle data using 8 harmonics. This is done at each of the four altitudes. The Fourier fits allow us to calculate mean daily temperatures as well as maximum and minimum temperatures removing the effects of oscillations and minor gaps in the data. Fits for each pair of sols are examined visually to filter out pairs of sols where calibration activities of TIRS or large data gaps may produce anomalous behaviors. In addition, the Fourier fits allow the thermal tide components of the diurnal thermal cycle to be examined.

Figure 7 shows the temporal evolution of daily mean temperatures (panel a) and the daily amplitude of the diurnal temperature cycle (maximum minus minimum, panel b) at each altitude up to sol 400 of the mission ($L_S \sim 13–203°$), together with some important drivers of temperatures, like the thermal inertia of the terrain (panel c) and the atmospheric opacity (panel d). Temperatures in panels a and b are compared with predictions from the LMD (Laboratoire de Météorologie Dynamique) Mars Global Climate Model (Mars GCM) used in Mars Climate Database (MCD; version 5.2) for a standard "climatology" dust scenario (Lewis et al., 1999). This comparison is further explored in Figure S4 in Supporting Information S1.

MEDA's mean temperatures at the surface, 1.45 and 40 m in Figure 7a are in good agreement with predictions from MCD (i.e., average difference below 1 K). MEDA data at 0.84 m are systematically warmer than MCD predictions by 2 K as a result of residual thermal contamination affecting ATS4-5 (see Section 2), especially at night. The progressive increase of temperatures observed at all levels as the summer advances (Figure 7a) follows closely the cycle of solar irradiance at the top of the atmosphere, with the daily average of the irradiance at the top of the atmosphere peaking at $L_S \sim 144°$ (sol 295) at Jezero, close to the peak in mean surface temperatures. A comparison of temperatures with irradiances is shown in Figure S5 in Supporting Information S1 using Equation 1 from Vicente-Retortillo et al. (2015) to calculate solar fluxes at Jezero.

The daily amplitude of the diurnal temperature cycle at each altitude is shown in Figure 7b for MEDA data and MCD predictions. The daily amplitude of the diurnal temperature cycle at the surface has strong changes in short timescales of a few sols that cannot be explained by seasonal evolution or by changes in the opacity of the atmosphere. These variations can only be explained by the motion of the rover over terrains with different properties.

Figure 7c shows thermal inertia and albedo values of the different terrains explored by Perseverance as a function of time. These values come from MEDA retrievals in Martínez et al. (2023), who uses a combination of TIRS and Radiation and Dust Sensor measurements. TIRS measurements characterize an area of 3 m², which is the FoV of its downward looking channel. Retrieved thermal inertia values along the rover traverse range from 180 to 605 J · m⁻² · K⁻¹ · s⁻¹ᐟ² (SI units), with a mean value of 351 ± 70 SI units (Martínez et al., 2023; Rodríguez-Manfredi et al., 2023). These values are comparable to orbital measurements with the Thermal Emission Imaging System (THEMIS) instrument obtained at a spatial resolution of 100 m (Fergason et al., 2006). Changes in TI correlate very well with observed changes in the surface temperature, and especially with its daily amplitude. Figure S6 in Supporting Information S1 shows the relation between the daily amplitude of surface temperature and the TI of the terrain. Both variables follow a linear relation with a linear regression coefficient of $r^2 = 0.76$. Terrains with low TI values experience higher amplitudes of surface temperatures over a sol, while high TI terrains experience much lower amplitudes. Similar variability of surface temperatures was reported in the region of Gusev crater explored by the Spirit rover due to inhomogeneous surface properties. By contrast, more uniform results were found in the region of Meridiani Planum explored by the Opportunity rover, which was more homogeneous in terms of such properties (Mason & Smith, 2021).

Changes in the thermophysical properties of the surface affect air temperatures only to a minor extent, and mostly at 0.84 m. Figures 7a and 7b show that the higher the altitude, the smaller the coupling between the atmosphere
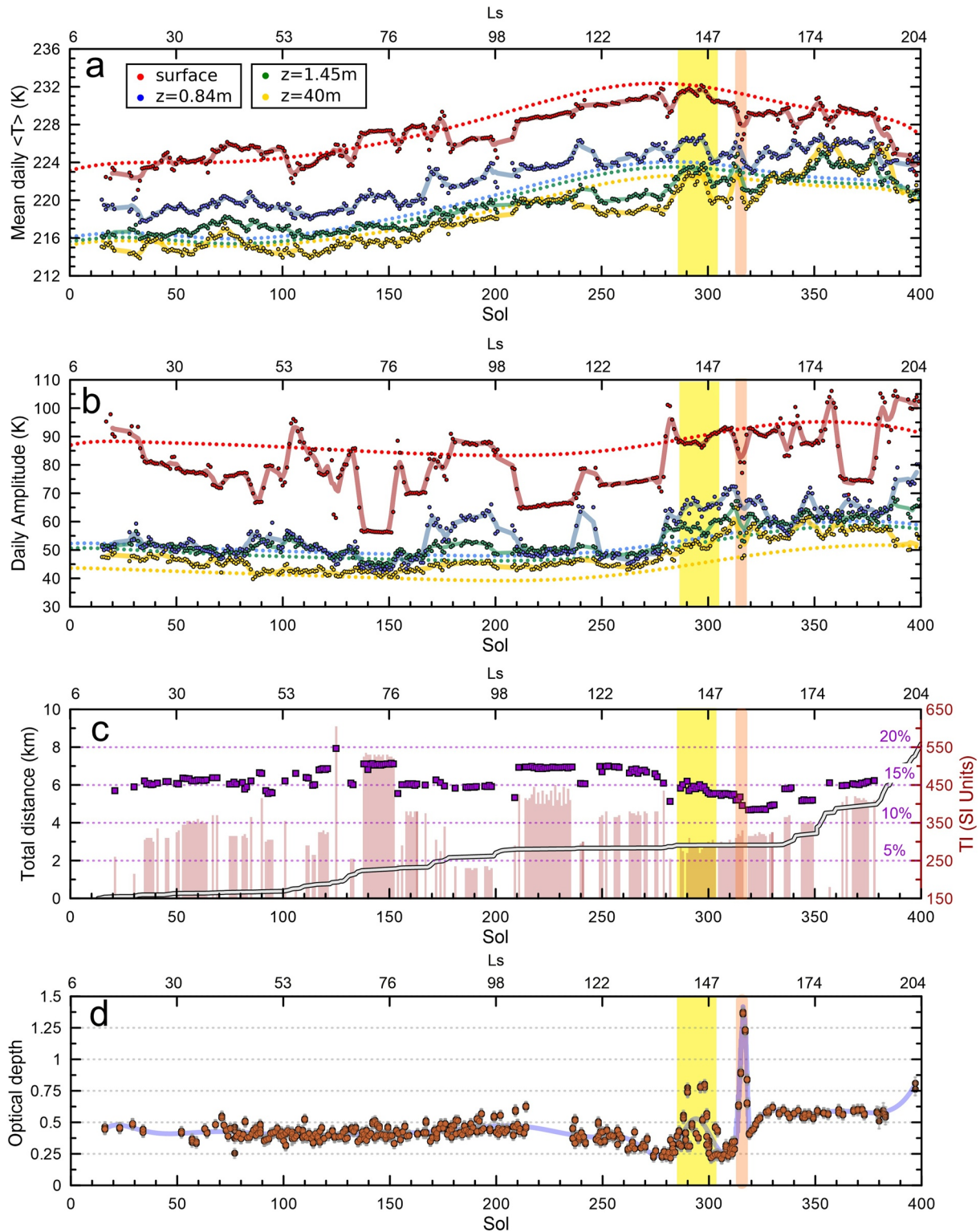
Figure 7. Temporal evolution of the mean daily temperatures at Jezero and the drivers of these changes. (a) Mean daily temperatures at four altitudes (colored dots, legend indicates altitudes for each color) for the first 400 sols ($L_S \sim 13$–$203°$). Solid lines are running averages of Mars Environmental Dynamics Analyzer data and dotted lines are temperature predictions from MCD. (b) Amplitude of the diurnal cycles. Colors and altitudes as in (a). (c) Distance traversed by the rover (white line, left axis), surface thermal inertia (red bars, right axis), and surface albedo (purple dots, dotted grid lines). (d) Optical depth from MastCam-Z measurements (symbol size is comparable to the error bar of the measurements). A smooth interpolation of the data is shown with a light-blue line. Regions shaded in yellow indicate a period of increased opacity. Orange shaded regions signal the regional dust storm period, $L_S \sim 152$–$156°$. Thermal inertia and surface albedo values are from Martínez et al. (2023). Dust opacities are from Bell et al. (2022).

and the short-term changes in surface temperatures associated with different terrains. The effect of the local TI becomes negligible in the mean daily temperatures at 1.45 and 40 m. This is because the measured atmospheric temperature corresponds to air masses that move horizontally over a broad heterogeneous terrain, averaging to a large extent the effects of the different surfaces.

Figure 7d shows the mean atmospheric opacity at Jezero measured by the MastCam-Z instrument in the visible range (Bell et al., 2022). These measurements have typical uncertainties of ±0.04 and correspond to the atmospheric column opacity produced by the combination of dust and clouds. The effects of atmospheric dust and clouds on the mean temperatures were small prior to the start of the dusty season (usually taken to begin at $L_S \sim 180°$). The atmospheric opacity, τ, was small ($\tau < 0.6$) except for increased opacities from sol 285 to 305 ($L_S \sim 139$–149°) and during the dust storm on sols 312–318 ($L_S \sim 152$–156°). These two periods when atmospheric opacity increased produced measurable effects on temperatures with clear increases of +4 K in mean daily air temperatures in the first case and more complex effects of the dust storm on temperatures as later discussed in Section 5.

4.2. Temporal Evolution of Temperatures as a Function of L_S and LTST

We now examine how temperatures evolve both as a combined function of L_S and LTST. Figure 8 shows temperatures at Jezero averaged in windows of 30 min as a function of L_S and LTST. In this figure, an interpolation over MEDA data in both L_S and LTST has been used to cover gaps in the data. We show ATS temperatures at 1.45 m (panel a) and surface temperatures from TIRS data (panel b), which are more reliable and have a lower number of gaps than temperature data at 0.84 and 40 m, respectively. The difference between surface temperatures and air temperatures at 1.45 m (panel c) constitutes a visualization of the evolution of the vertical thermal gradient at different hours through the 400 sols.

Overall, both daytime temperatures at the surface and at the 1.45 m level followed the solar insolation cycle: starting with lower values and increasing with L_S as summer and maximum local insolation approached. Daily air temperatures increased only slightly over the first 280 sols of the mission, consistent with the very slow increase of solar irradiance at the top of the atmosphere over that time period (Figure S5 in Supporting Information S1). Later, around sol 280, air temperatures increased sharply coinciding with the sudden increase in atmospheric opacity observed at Jezero (Figure 7d). Air temperatures remained high since then, despite short-term decreases in atmospheric opacity. The highest air temperatures were measured during the dust storm on sols 313–315. The peak solar irradiance at local noon occurred on sol 335 ($L_S = 165°$) but temperatures stayed high up to sol 400 in parallel with slightly higher values of dust opacity measured during this period. The effects associated with the dust storm were complex and are detailed in Section 5.

Surface temperature measurements experienced strong influences from the surface TI, resulting in sharp discontinuities in the map of surface temperatures (Figure 8b). These effects are partially transmitted to the atmospheric temperatures at 1.45 m, for example, at $L_S \sim 75°$, but are minimized when computing mean daily temperatures. These changes in both surface and air temperatures did not lead to important changes in the amplitude of temperature fluctuations.

Figure 8c shows the difference between surface and air temperatures at 1.45 m. These are dominated by the changing surface temperatures, which in turn depend primarily on the TI of the local surface. As highlighted in Figure 8c, Perseverance was located on terrains with anomalously high values of TI for several sols. In those cases, nighttime temperatures resulted in a breakdown of the nighttime thermal inversion, mainly related to nighttime warm surface temperatures. Although this result contradicts previous observations of nighttime thermal inversions (Miller et al., 2018; Schofield et al., 1997; Smith et al., 2004) and is against atmospheric models of Jezero (Newman et al., 2021; Pla-García et al., 2020), it is only a local effect. While surface temperature is retrieved locally from a 3 m² FoV, air temperatures are dependent on average surface properties over a much larger region (Rodríguez-Manfredi et al., 2023; Savijärvi et al., 2022).

4.3. Thermal Tides and Long-Period Waves (>1 sol)

4.3.1. Thermal Tides

Thermal tides are an integral part of the Martian meteorology (Barnes et al., 2017; Leovy, 1977; Rafkin et al., 2017). They are typically investigated via their effects on surface pressure (Guzewich et al., 2016) or on
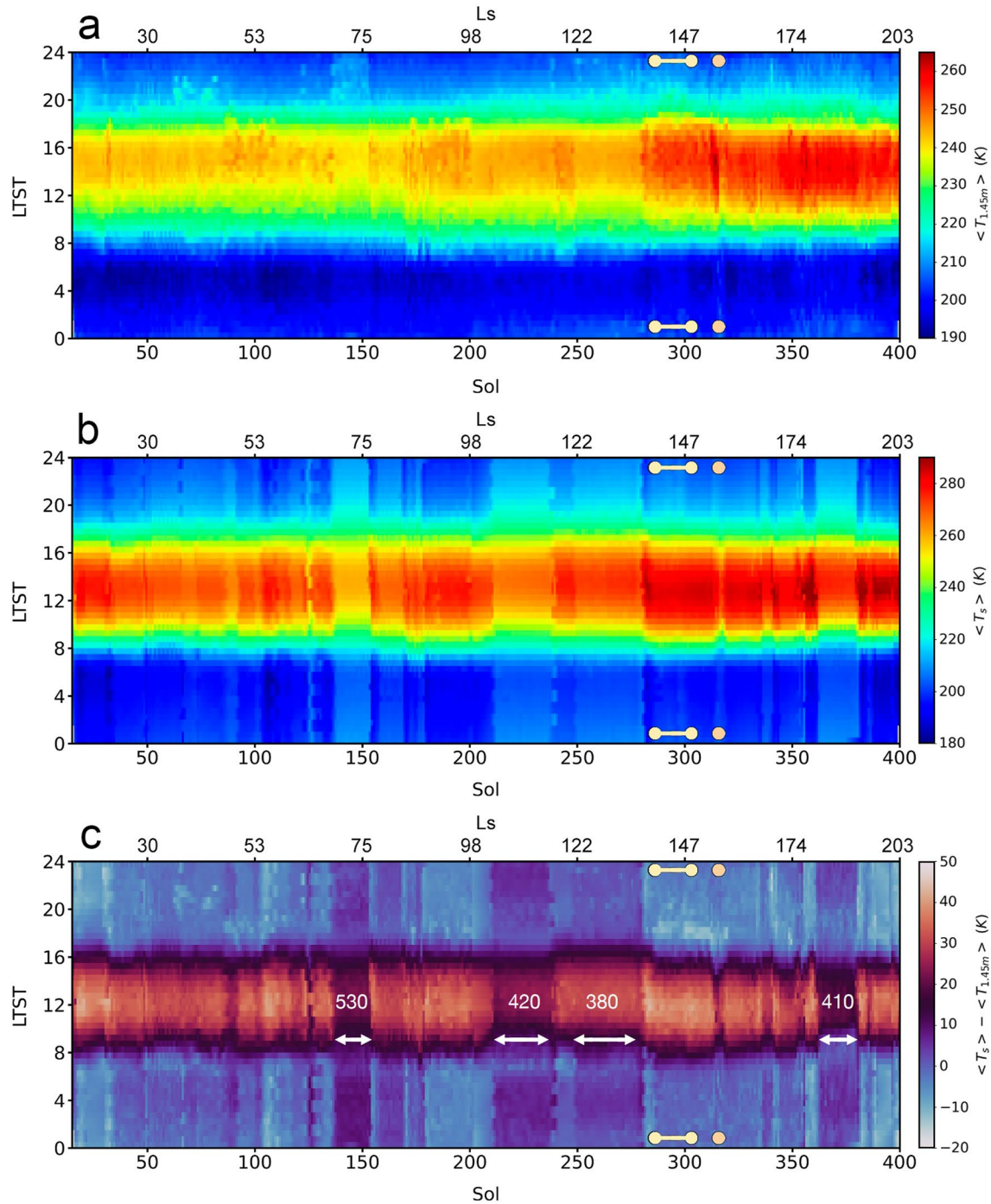
Figure 8. Interpolated temperatures at Jezero as a function of L_S and Local True Solar Time (LTST). (a) Air temperatures at 1.45 m. (b) Surface temperatures. (c) Surface temperatures minus air temperatures. Note the different temperature ranges used in panels (a and b). Temperatures were calculated using 30 min averages and interpolated in L_S and LTST using triangular interpolation to mask gaps in the temporal coverage. White numbers in panel (c) indicate the TI values of different high TI terrains, while the arrows show how long the rover was parked at the same site. TI values from Martínez et al. (2023). Connected circles show the start and end of a period of increasing opacity, and a single circle and its diameter show the time and duration of the dust storm.

temperature maps of the atmosphere at different altitudes obtained from orbit (Banfield et al., 2000). The study of thermal tides using temperature time series (rather than pressure) from weather stations on the surface of Mars is uncommon in the literature. This is because the Martian atmosphere has a low thermal inertia and the near-surface temperatures are mainly controlled by the diurnal and seasonal cycles of solar irradiance (affected

by local properties such as the atmospheric opacity and properties of the surface) and not so much by the horizontal transport of weather systems. Thus, the diurnal tide with a period of 24hr is expected to be the strongest mode with a nearly constant phase. Temperature variations on different sols are associated with the slow seasonal evolution or with local atmospheric dust abundances, while effects on temperatures from atmospheric waves and weather systems may only present small amplitudes. This is different to what is found in Fourier analyses of surface pressure in which significant contributions of the semidiurnal and higher order tides, including migrating waves, combine to shape the daily behavior of pressure, which can vary considerably over different sols (Guzewich et al., 2016; Sánchez-Lavega et al., 2023).

A Fourier transform of temperatures at 1.45 m for each consecutive pair of sols results in a series of harmonic terms in which the diurnal cycle can be decomposed. The following equation defines the series:

$$T(t) = A_0 + \sum_{k=1}^{N} A_k \sin\left[(kt + \phi_k) * (2\pi/24.0)\right], \tag{1}$$

where $T(t)$ is temperature as a function of time, t, k is an index expressing the number of the harmonic, ϕ_k is the phase of the harmonic k, A_k are the amplitudes of the different harmonic terms, and A_0 represents the daily mean value of temperatures. In this expression, both t and ϕ_k are expressed in LTST hours.

Figure 9 shows the amplitudes and phases of the first few modes for temperatures at 1.45 m. Similar analyses can be performed for other atmospheric levels but lead to noisier results. The vast majority of the daily thermal structure at 1.45 m is explained by the first two Fourier terms (diurnal and semidiurnal modes), with both having nearly constant amplitude and phases at least up to sol 280 ($L_S \sim 136°$). The nearly constant phase of 15 hr of the first harmonic is close to the daily maximum of temperatures, and the contributions from additional harmonics move the daily maximum toward slightly different times of the sol. After sol 280, the increasing amount of atmospheric aerosols and optical depth seems to have impacted temperatures, notably changing the amplitude of at least the first and the second Fourier components.

The strongest changes in amplitudes and phases of the Fourier series of temperature were found during the January 2022 regional dust storm on sols 312–318 (Section 5), with a reduction of the diurnal component and an increase of the semidiurnal component. After the dust storm, changes in the diurnal thermal cycle continued to occur, and the relative amplitude of the semidiurnal mode increased, along with a decrease of the terdiurnal mode. These changes are related to a different shape of the diurnal cycle of temperatures, which has a flatter structure during the hours of higher irradiance over the late summer. A similar situation is observed in the pressure field with an increase of the diurnal and semidiurnal modes after sol 300 (Sánchez-Lavega et al., 2023).

4.3.2. Long-Period Waves (Period >1 sol)

We next examine the excursions of mean daily temperature on timescales between diurnal and seasonal. Oscillations in atmospheric variables on timescales larger than a sol are generally related to planetary scale waves or the passage of weather fronts. Battalio et al. (2022) examined planetary waves from multiple meteorological variables measured by Perseverance and MSL, including temperatures, and compared their results with the Ensemble Mars Atmospheric Reanalysis System (EMARS) data set. According to this work, traveling waves of baroclinic nature with periods of ∼3 sols are found in the temperature data from Perseverance, MSL, and EMARS, being further supported by their analysis in pressure, whereas waves with periods above 8 sols are attributed to barotropic instabilities and possible weather fronts.

We study oscillations in mean daily temperatures from MEDA ATS data at 1.45 m and MCD predictions. For this analysis, the MCD data set differs from the one in Figure 7. The MCD data shown here reconstructs the effects of large-scale perturbations on a typical Martian year adding synthetic perturbations to the averages of Mars GCM simulations that define the MCD. These perturbations are added using Empirical Orthogonal Functions (EOFs) that are calculated from the original Mars GCM simulations and that are representative of the typical variations in the Mars GCM. EOFs are a statistical technique that examines the covariance of atmospheric variables in the Mars GCM as a function of both height and longitude generating a set of functions and coefficients that are later used to reconstruct the typical effects of large-scale perturbations in the model (Lewis et al., 1999; Millour et al., 2017).

For both MEDA and MCD, we fit and subtract a seventh-degree polynomial to the mean daily temperature at 1.45 m between L_S 13° and 203°. Figure 10a shows the two time series of the oscillations of mean daily temperature from which the seasonal evolution has been removed. The time series of MEDA data shows variations
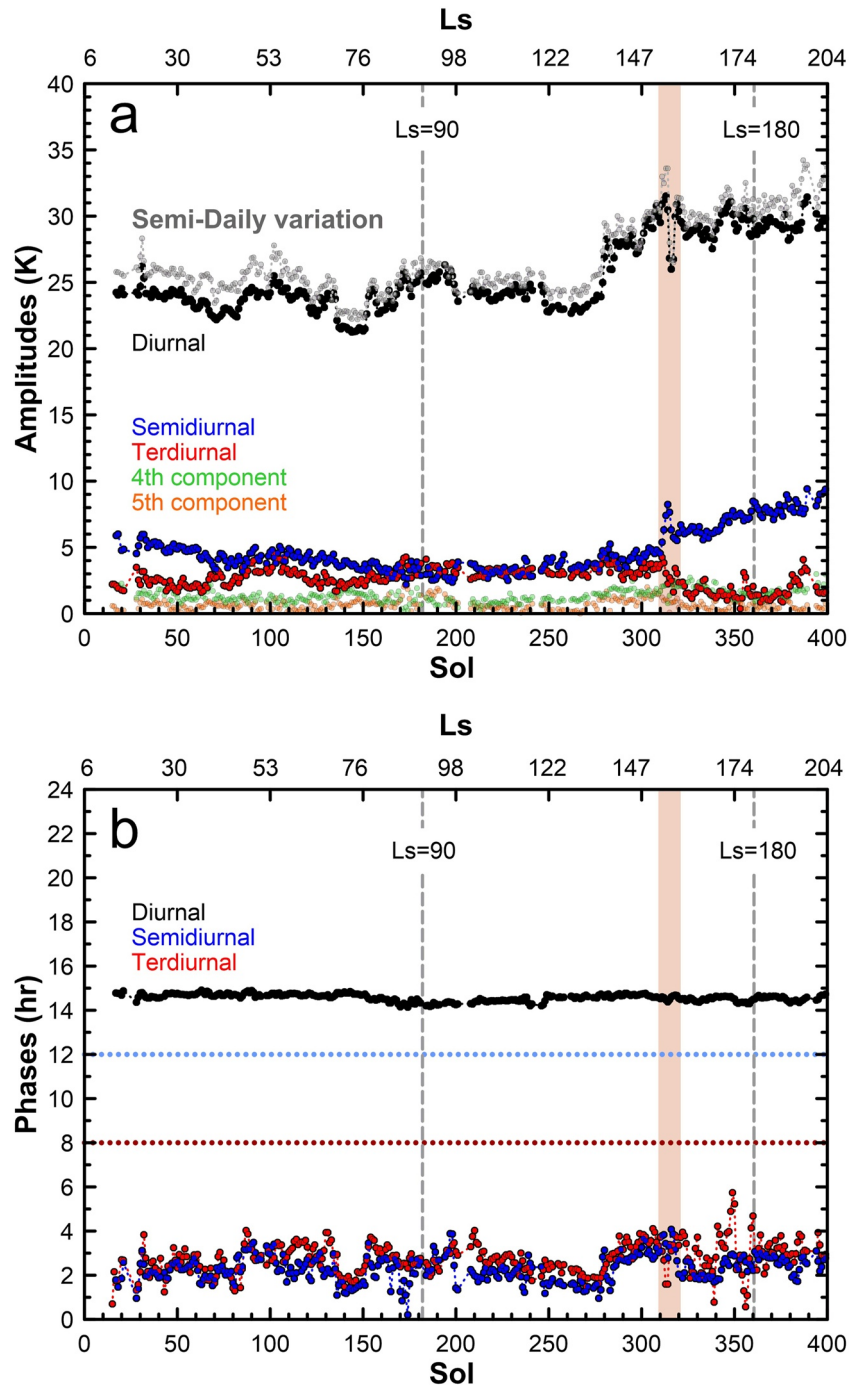
Figure 9. Thermal tides at 1.45 m. (a) Amplitudes of the first five Fourier terms. Gray dots show the semi-diurnal amplitude of temperatures (($T_{max} - T_{min}$)/2) at 1.45 m. (b) Phases of the thermal tides (only the first three components). Horizontal lines represent the maximum phases for each mode (12 hr for the semidiurnal mode, blue-dotted line, and 8 hr for the terdiurnal mode, red-dotted line). Vertical dashed lines indicate the northern hemisphere Summer Solstice ($L_S = 90°$) and Autumn Equinox ($L_S = 180°$).

of ±1 K with a superposition of fast (periods of about 3–9 sols) and slow cycles (periods of about 40 sols) and isolated peaks associated to the times of strong variations in dust opacity after sol 280. The MCD time series is qualitatively similar, although it is based on a statistical description of Mars GCM simulations reconstructing typical variations for Jezero at that seasonal period. Note that thermal oscillations in MEDA and MCD have similar amplitudes (1 K) to those identified by Battalio et al. (2022).
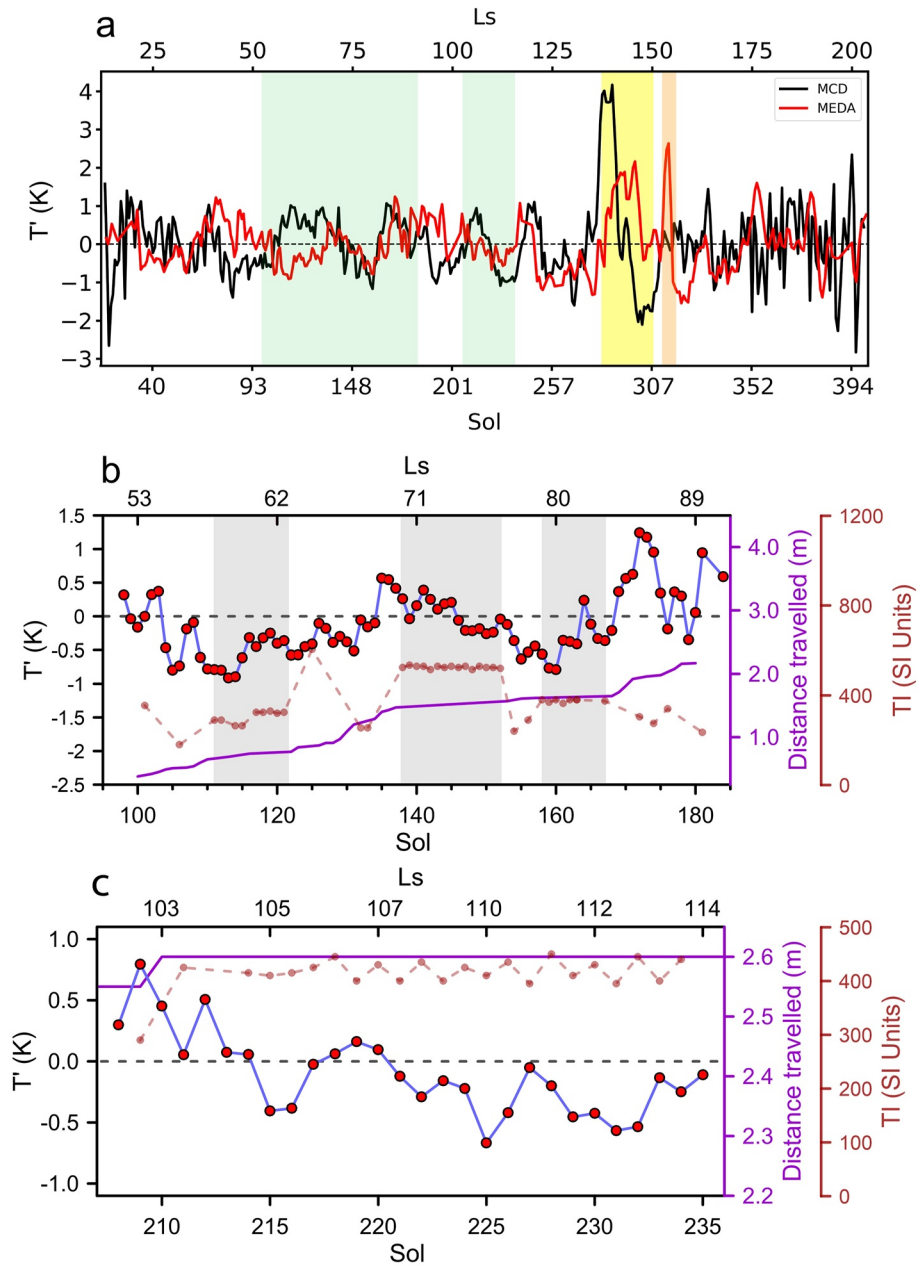
Figure 10. Daily oscillations in mean temperature from Mars Environmental Dynamics Analyzer (MEDA) temperatures at 1.45 m for three periods of interest: sols 15–400 (a), sols 96–182 (b), and sols 208–235 (c). A seventh order polynomial has been fit and removed from the mean daily temperature data over the first 400 sols of the mission. Panel (a) displays the MEDA data in red, and MCD predictions that account for large-scale perturbations in black. Note that both time series share similar features. The regions shaded in yellow and orange indicate a time of increasing opacity and the regional dust storm, respectively. The two sol ranges shaded in green are zoomed in panels (b and c). In these panels, temperature departures from the polynomial fit to the data are shown as red dots connected by blue lines. The orange-brown dots display the TI of the terrain (the shaded periods in (b) correspond to nearly constant surface TI values) and the purple line shows the total distance traveled by the rover.

To assess the influence of the surface thermal inertia, Figure 10b displays the thermal oscillations over a portion of the complete time series. The range of sols covered here has nearly constant dust opacity but varying properties of the surface TI (with a nearly constant albedo of 0.13 ± 0.01) as the rover moves over the terrain. The ranges of sols shaded in the figure correspond to times with nearly constant TI and show thermal oscillations of about 0.2 K with maximum amplitudes of 0.5 K. The mean periods of these oscillations are difficult to assess

but the general structure of the oscillations seems to be uniform despite the large changes in TI. This supports the search for large-scale atmospheric wave effects in MEDA temperature data. Isolated peaks in Figure 10a could be representative of the passage of weather fronts. A similar analysis over the longest set of sols with no rover motion and similar environment characteristics (Figure 10c, with local albedo of 0.137 ± 0.006) also shows equivalent thermal oscillations, with amplitudes lower than 0.5 K and periods from 3 to 9 sols with no isolated peaks.

The periodicities of a few sols observed in Figure 10c are compatible with those of baroclinic waves, that is, traveling waves that originate in baroclinic instabilities at midlatitudes and high latitudes and extend down to low latitudes, resulting in oscillations in pressure, winds, and temperatures (Charney, 1990). On Mars, baroclinic waves have been identified several times in time series analyses of surface pressure data since the Viking Landers (Banfield et al., 2020; Barnes, 1980; Haberle et al., 2018). However, before MEDA, oscillations in near-surface air temperatures due to baroclinic waves have only been demonstrated at the landing site of VL2 at 48°N (Barnes, 1980), where baroclinic waves with similar phases and periods were found in pressure, wind, and near-surface temperature data, with periods from 3 to 6 sols. With MEDA, the effects of baroclinic waves have been identified in the time series of pressure data over the first 460 sols of the mission, with a strong increase in activity after the start of the dusty period on sol 280 (Sánchez-Lavega et al., 2023). While temperature data between sols 280 and 400 present strong variations in the mean daily temperature, the interpretation of these variations is more complex due to the changing dust opacity combined with the frequent drives of the rover in this phase of the mission.

Thus, our analysis suggests that planetary waves at Jezero crater are detectable from MEDA air temperature data, with periodic variations that are qualitatively similar to model expectations (Figure 10a) and to results from the pressure sensor (Sánchez-Lavega et al., 2023).

5. Thermal Effects of a Regional Dust Storm From $L_S \sim 153–156°$

A large regional dust storm arrived at Jezero on sol 312 (5 January 2022) and remained active until sol 318 (spanning $L_S \sim 153–156°$). The storm was followed by a rapid return to the previous environmental conditions after the dust storm ceased. During this event, Perseverance was located on the *Issole* sample-collection site, where it stayed from sol 286 to 327, which allows us to measure the impact of the dust storm on meteorological variables without the complication of different terrains. Lemmon et al. (2022) presents an in-depth analysis of the dust storm, the evolution of dust opacities, and the effects on the surface. Here, we offer a closer look to the evolution of temperatures. For context, the optical depth of the atmosphere in the visible range increased from $\tau = 0.28 \pm 0.07$ before the dust storm (sols 300–311) to 1.4 ± 0.04 at its peak (sol 316), and returned to moderate values ($\tau = 0.44 \pm 0.04$) after the storm ceased (sols 319–322) (Lemmon et al., 2022).

Figure 11 shows the evolution of temperatures at 1.45 m and at the surface over the period of development of the dust storm. Data from sols 310, 311, 320, and 321 (i.e., prior to and following the storm) are representative of average atmospheric conditions at $L_S \sim 154°$ without effects associated with the dust storm. During the sols when the dust storm impacted Jezero, air temperatures increased by 12 K near 14:30 LTST, with maximum air temperatures reached on sol 314 ($\tau = 0.64 \pm 0.04$). Nighttime temperatures increased throughout the dust storm, with minimum daily temperatures at around 06:00 LTST increasing by 6–8 K from the surface to the 40 m level. Daytime surface temperatures were not affected on sol 312, when the dust storm arrived to Jezero, but later decreased progressively with minimal values on sol 316 ($\tau = 1.4 \pm 0.04$), reducing the maximum surface temperature at noon by 9.5 K.

The overall changes produced by the dust storm can be observed in the evolution of the maximum and minimum daily temperatures, which are shown in Figure 12 compared with the evolution of the maximum thermal gradients, which typically occurred at around 10:30–11:00 LTST. This figure evidences a phase shift of at least 1 sol in the thermal response of the atmosphere and the surface, which reacted later to the effects of the dust storm. This shift in the thermal response of the air and surface temperatures suggests the arrival of a warm air mass accompanied by low altitude dust absorbing more daytime radiation and mitigating nighttime cooling.

The gradual decrease of surface temperatures during the first few sols of the dust storm, combined with the warm air, resulted in a reduction of the thermal gradient of the ASL at noon on sols 314–318. However, during the first few sols of the storm there was strong convective activity in the form of frequent wind gusts and dust devils on sols 312–315 (Hueso et al., 2023; Lemmon et al., 2022). Lemmon et al. (2022) observed a reduction of low-level
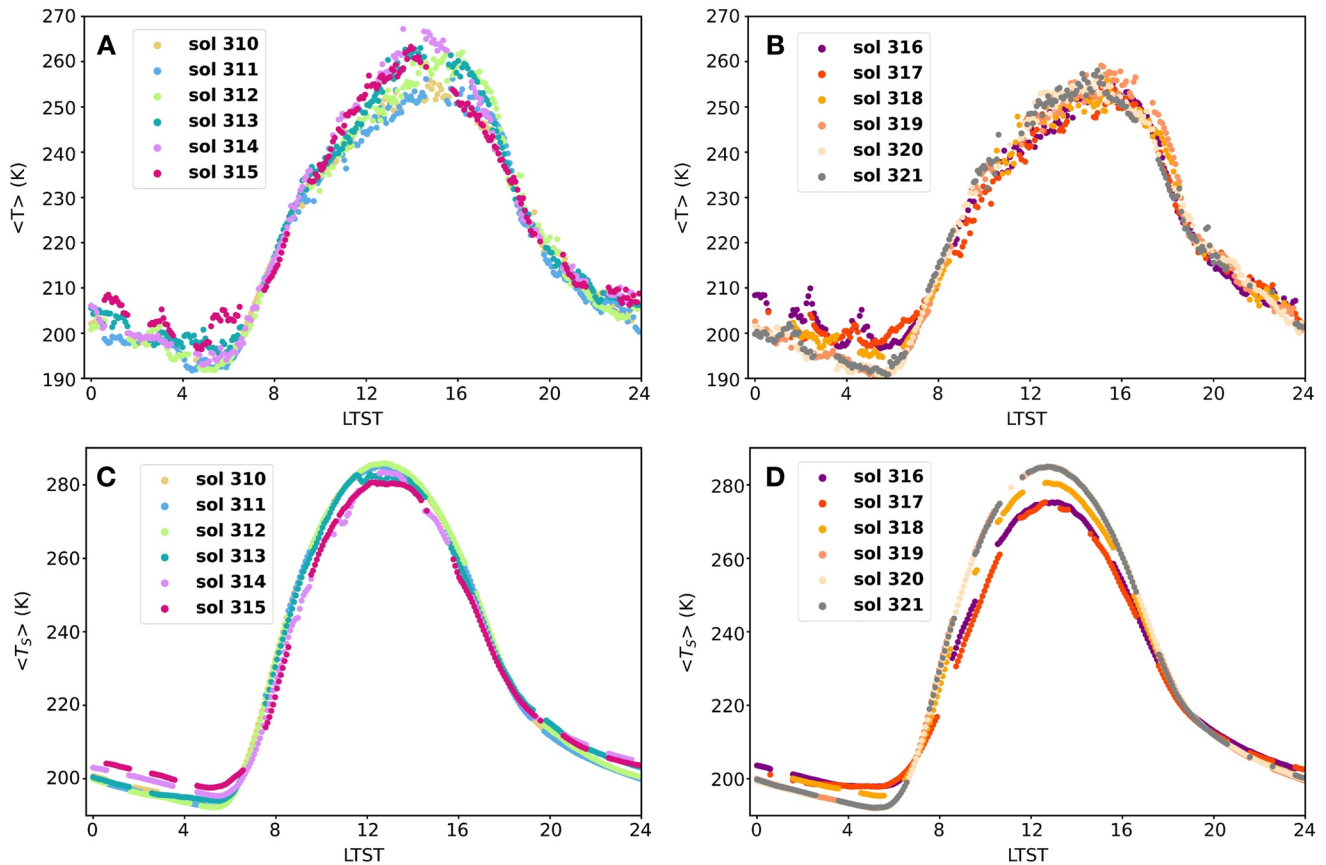
Figure 11. Air and surface temperatures during the L_S = 153–156° dust storm. (a and b) Air temperatures at 1.45 m. (c and d) Surface temperatures. Dots represent 5-min averages of temperatures for each sol.

dust on sol 316, and Vicente-Retortillo et al. (2022) indicate that the largest sol-to-sol variation in surface albedo occurred between sols 315 and 316 with a decrease in albedo of 11%. These two works suggest a change in the vertical dust profile at Jezero in the evening of sol 315. In addition, we observe a rapid cooling of maximum air and surface temperatures on sol 316 and thereafter, accompanied by a recovery of normal surface and air temperatures after the storm (Figure 11). The changes in the vertical distribution of the dust between sols 315 and 316 might have been driven by the strong reduction in the vertical thermal gradient on sols 314–315 (Figures 12c and 12d) producing a negative feedback on the maintenance of vertical motions and storm activity.

The thermal effects observed during this dust storm can be compared with in situ data during previous dust storms. Two Global Dust Storms (GDS) were observed by the Viking Landers on MY12. These storms reached atmospheric dust opacities of $\tau = 3$ and $\tau = 6$, respectively (Pollack et al., 1979), and maximum air temperatures were observed to decrease by ∼19 K (Ryan & Henry, 1979). The REMS instrument on the Curiosity rover obtained meteorological data of the 2018/MY34 GDS, which reached values of $\tau \sim 8.5$ and resulted in decreases of surface and air temperatures of 35 and 30 K, respectively (Guzewich et al., 2019; Viúdez-Moreiras et al., 2019). Streeter et al. (2019) studied this GDS combining numerical modeling and data from the Mars Climate Sounder. They found a complex set of effects on surface and air temperatures at different locations. According to Streeter et al. (2019), heterogeneous changes in temperatures are expected during a dust storm as a consequence of nonuniform terrain, nonuniform structure of the dust storm, and changes in surface albedo and TI created by dust deposition and dust lifting. For example, the regions of extremely low thermal inertia terrains ($TI < 100$ SI units) presented an average daily warming of surface temperatures, which reduced vertical thermal gradients and coupled more strongly the surface and the atmosphere. In contrast, the regions of middle to high surface TI values presented a cooling of surface temperatures, in agreement to our observations at Jezero.

Large regional dust storms were observed by Spirit and by InSight ($\tau \sim 1.9$), resulting in surface temperature decreases of about 10 K but with no perceptible variations in maximum air temperatures (Smith et al., 2006;
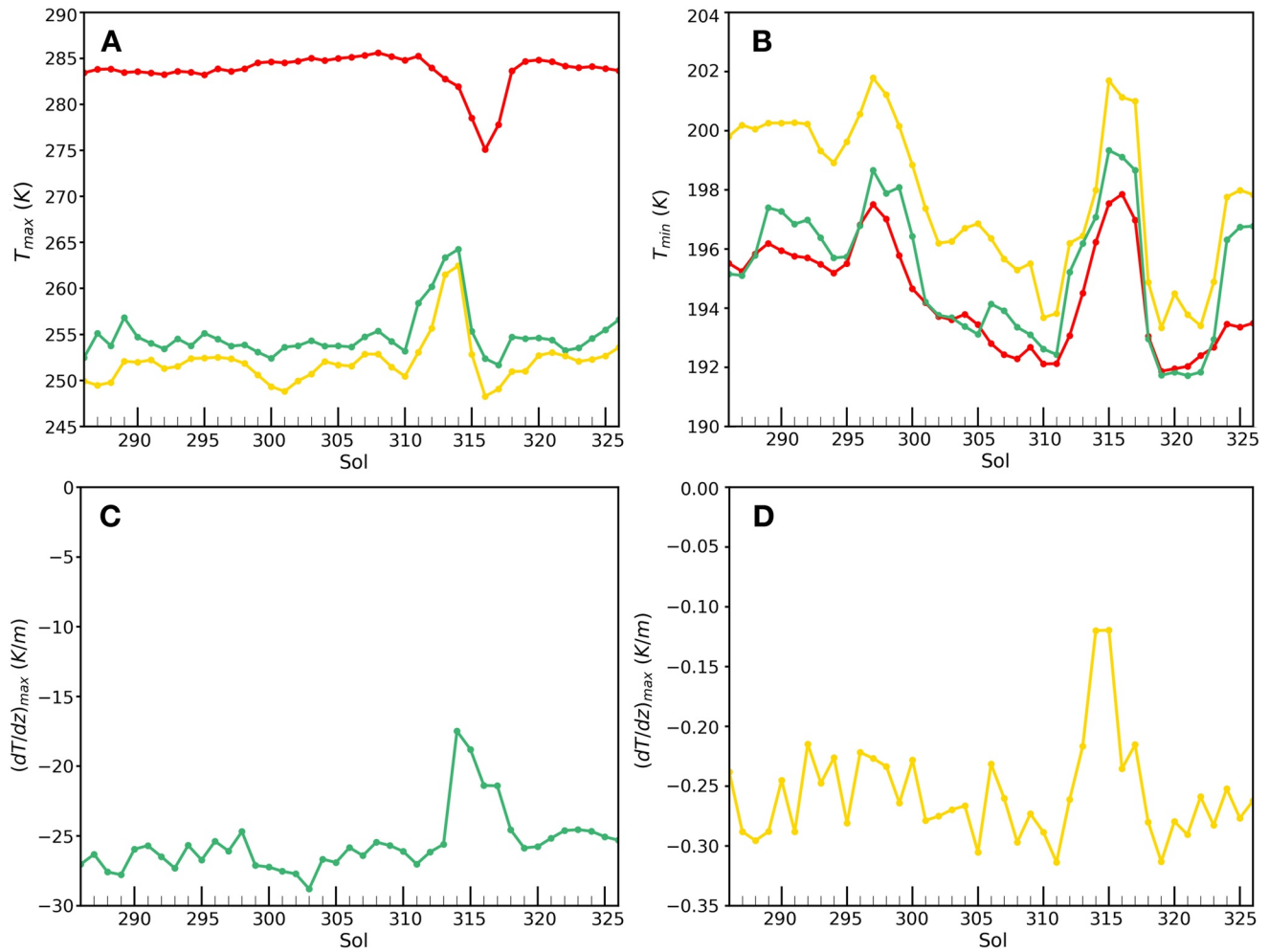
Figure 12. Evolution of the daily maximum (a) and minimum (b) temperatures. Red, green, and yellow identify the surface, the 1.45 m level and the 40 m level, respectively. Panels (c and d) show the daily maximum thermal gradients between the surface and 1.45 m and between 1.45 and 40 m, respectively, and correspond to near noon conditions. Each value shown in the figure is actually constructed using data from two consecutive sols (the indicated sol and the next one) to remove effects from gaps in the data.

Viúdez-Moreiras et al., 2020). Ordonez-Etxeberria et al. (2020) studied a local dust storm with MSL data and reported that while the maximum surface temperature decreased during the passage of the storm, the atmospheric maximum temperatures increased by 14 K. Thus, the local storm observed by MEDA at Jezero offered a closer resemblance to the one observed by MSL, although the local storm was smaller in size and duration with only one sol in which the storm reached $\tau = 1.6$.

6. Comparison With Previous Missions and Model Predictions

6.1. Comparison With Previous Missions

Several surface missions (VL1, VL2, MPF, PHX, M2020, and InSight) have recorded near surface atmospheric temperatures on Mars (Banfield et al., 2020; Davy et al., 2010; Gómez-Elvira et al., 2014; Hess et al., 1977; Martínez et al., 2017; Schofield et al., 1997; Sutton et al., 1978). Of all these missions, only VL1 and MPF obtained data at latitudes comparable to that of Jezero (at latitudes between 18 and 22°N).

Figure 13 shows daily averaged air temperatures from Mars 2020 compared with VL1 and MPF. During the brief period of time it was active, MPF obtained temperature data that resemble those of Mars 2020. Temperature data of Mars 2020 and VL1 show that Mars 2020 temperatures are systematically higher than those of VL1 by ~6.5 K. This difference is well above the uncertainty in absolute temperatures of both missions, which is 1.0 K for MEDA
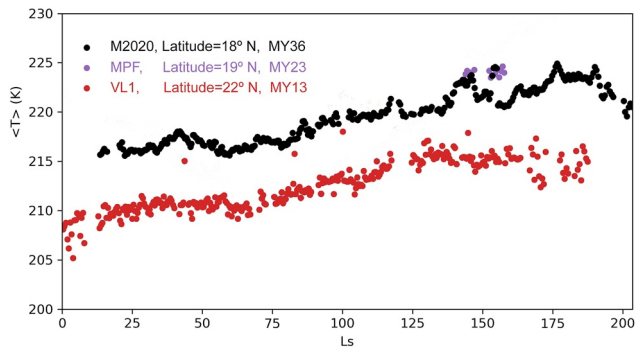
Figure 13. Daily averaged air temperatures as a function of L_S for VL1, MPF, and Mars 2020. Data from VL1 and MPF come from the multimission comparative analysis by Martínez et al. (2017) and only include sols with full diurnal coverage to get accurate mean daily temperatures.

(Rodriguez-Manfredi et al., 2021) and 1.5 K for VL1 (Hess et al., 1977), and we now examine differences between these locations that can explain this temperature difference.

For both Mars 2020 and VL1, dust opacity values were moderate and close to 0.5 during most of the period from $L_S = 0$–180° (Pollack et al., 1977; Rodríguez-Manfredi et al., 2023) (at the VL1 landing site we consider data from only MY13 because a GDS affected results in MY12). The elevations of the landing sites of VL1 (−3.6 km), MPF (−3.7 km) and Mars 2020 (−2.7 km) are not expected to play a major role in modifying air temperatures, since Martian atmospheric temperature is radiatively controlled rather than convectively (as on Earth), and hence the elevation-pressure difference should not significantly affect temperatures. Each mission obtained temperature measurements from sensors at different altitudes relative to the surface. The VL1 and MPF temperature sensors considered here were located at 1.6 and 1.27 m above the surface, respectively. These differences in altitude are relatively small (note that most of the vertical thermal gradient in the ASL is concentrated in the lower meter) and cannot explain the 6.5 K difference between VL1 and Mars 2020.

There is, however, a substantial difference in surface albedo between the VL1 and Mars 2020 landing sites. Perseverance's trajectory over Jezero is characterized by an albedo of 0.12 ± 0.01 (Martínez et al., 2023), whereas VL1 landed in a region with an albedo of ~0.24 (Christensen, 1988). This is consistent with more radiation being absorbed by the surface at Jezero and therefore heating further the local atmosphere. In contrast, the average surface TI from THEMIS data (Fergason et al., 2006) is similar at the two sites: 380 and 350 SI units for VL1 and Mars 2020, respectively. Also note that TI variations are not expected to drive changes in average temperatures, whereas the albedo is expected to do so (Kieffer et al., 1977). In addition, we note that in Schofield et al. (1997) the difference in temperatures between MPF and VL1 was attributed to a lower albedo of the MPF landing site compared with that of VL1.

6.2. Model Comparisons With MEDA Data

Multimodel predictions of the meteorological conditions at different L_S in Jezero were compiled by Newman et al. (2021) and Pla-García et al. (2020). Figure 14 offers a direct comparison of the diurnal thermal cycles at Jezero at $L_S = 90°$ predicted by some of those models, MEDA measurements and climatic data from MCD (v5.2). MEDA-MCD comparison of mean daily temperatures can be further examined in Figure 7 and Figure S4 in Supporting Information S1.

Overall, model predictions closely approach MEDA measurements of temperatures, with differences mainly related to the spatial resolution at which models consider the heterogeneous TI and albedo of the terrain. For instance, the MEDA data shown in Figure 14 corresponds to measurements over a low TI terrain (240 SI Units) with low albedo (0.117 ± 0.006) compared to the values used by the Mars Weather Research and Forecasting Model (MarsWRF) (261 SI Units and albedo of 0.134) or the local values considered in the Mars GCM used in MCD (319 SI Units and albedo of 0.165).

Figure 14a shows that MarsWRF underestimates maximum surface temperatures by about 10 K and minimum temperatures by a few K at $L_S = 90°$. Model results at 0.84 m in Figure 14b are only available for MCD, which interpolates temperatures from the lowest resolved layer down to the surface. MEDA data at 0.84 m closely approach MCD data over most of the sol. However, there are evidence of thermal contamination on MEDA data at this level at 14–19 hr LTST. MEDA temperatures are higher in that range than MCD and show almost null temperature fluctuations, which is a sign of both sensors not being coupled enough to the environment. This thermal contamination is due to heating of the rover front side by the afternoon Sun with the incoming wind direction being blocked by the rover body at that time (see Appendix A). Model and MEDA data at 1.45 m in Figure 14c show similar differences and levels of agreement that the comparison at the surface. Finally, while most models do not produce output at the 40 m level sampled by TIRS, Mars Regional Atmospheric Modeling System (MRAMS) temperatures at 15 m (using a TI of 260 SI Units and albedo of 0.136) approach extremely
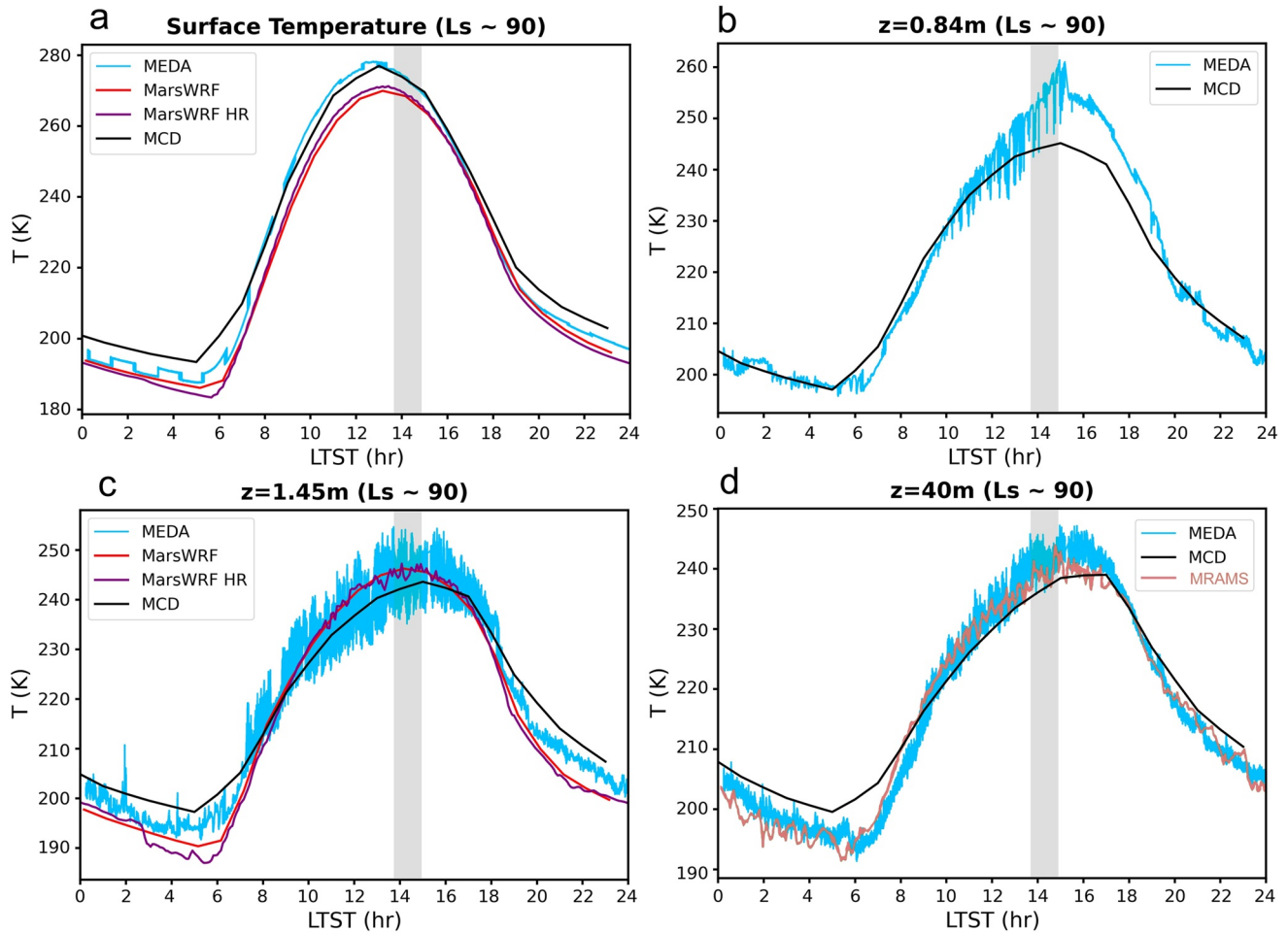
Figure 14. Comparison of Mars Environmental Dynamics Analyzer (MEDA) temperatures with model predictions for $L_S = 90°$. MEDA data comes from sols 180 and 181, where the surface TI is 240 SI units and the albedo is 0.117. Shadowed areas show the time of a drive of 458 m on sol 180 with little to no effect on temperatures. (a) Surface temperature; (b) air temperature at 0.84 m; (c) air temperature at 1.45 m; and (d) air temperature at 40 m. The smooth behavior of surface temperatures over the drive period indicates a drive over a terrain with nearly constant thermophysical properties.

closely the MEDA measurements at 40 m (in this altitude range, temperature differences over a few tens of meters are very small). Thus, taking into account precise values of surface albedo and TI can result in excellent matches of model data and MEDA measurements (see Savijärvi et al., 2022).

From a more general perspective, in both MEDA data and models, daily maximum temperatures vary considerably across seasons, whereas the minimum temperatures are quite stable. While these MEDA data and model comparisons are made using prelanding simulations, we expect their agreement with MEDA data to improve substantially in the future by incorporating the main features of heterogeneous terrain and atmospheric optical depth. Those comparisons will probably result in new insights into the essential factors controlling surface and atmospheric temperatures in the Jezero region, and across Mars in general.

7. Conclusions

The MEDA instrument is providing a rich data set of temperatures at four altitudes from the surface up to around 40 m. Temperature data at 0.84 m contain some thermal contamination ($\sim+2$ K) from the rover body but thermal contamination effects are much reduced at all other levels, enabling a detailed examination of temperatures through the ASL at Jezero. Below, we summarize our main findings from the analysis of the first 400 sols of the mission ($L_S \sim 13$–$203°$):

- The diurnal cycle of temperatures at Jezero is characterized by strong daytime convective activity that generally starts well after sunrise at about 07:30 LTST and vanishes well before sunset at around 17:00 LTST. At

that time the near-surface atmosphere becomes isothermal and temperature fluctuations vanish, marking the collapse of the CBL.

- The seasonal evolution of temperatures at Jezero was small over the period studied. This is a consequence of the tropical location of Perseverance and the small variations in solar irradiance and atmospheric opacity during the period studied. Mean daily temperatures at the surface and at the atmospheric levels studied are generally close to climatic values from MCD, except for the 0.84 m level, which is affected by its sheltered location and generally gives mean daily temperatures that may be artificially elevated by ∼2.0 K.

- The amplitudes of the diurnal cycles of surface temperature are very variable with values that range from 55 to 105 K, depending on the thermal inertia of the terrain, the season, and the atmospheric opacity. The amplitudes of the diurnal cycles of atmospheric temperatures from 0.84 to 40 m vary from 40 to 65 K, depending mainly on seasonal effects (slight increase from summer to autumn).

- A nighttime thermal inversion is observed on most sols in agreement with model predictions for Jezero. The intensity of the thermal inversion weakens slightly through the night in the first 40 m because of different cooling rates of the surface and atmosphere. Over terrains of high thermal inertia, the local nighttime thermal inversion appears to be broken. We interpret this as a local situation that arises from having surface temperatures that can be representative of surface thermophysical properties averaged over small spatial scales, in contrast to air temperatures at different levels, which are dependent on the average surface properties of a larger region.

- The near-surface atmospheric temperatures change slightly from sol to sol. Temperature oscillations of less than 1 K in the mean daily temperature appear both in the MEDA data set and MCD predictions and are interpreted as signatures of planetary waves, but further analysis is needed over a full Martian year. A Fourier decomposition of the diurnal temperature cycles results in diurnal and semidiurnal mode amplitudes of ∼25 and 4 K, respectively, with a very constant behavior and little suggestion of nonlocal effects on temperatures. However, the arrival of a regional dust storm at Jezero produced significant changes in the diurnal cycle of temperatures and its periodic components.

- The intensity of atmospheric temperature fluctuations peaks near noon, closely following the thermal gradient between the surface and the atmosphere. Temperature fluctuations are strong at 1.45 m ($\sigma_T \sim 2.5$ K with peak values of 11 K) and are significantly weaker at 40 m ($\sigma_T \sim 1.4$ K with peak values of 8 K). This vertical decay of the amplitude of temperature fluctuations is likely caused by vertical mixing over that altitude range.

- The January 2022/MY36 $L_S \sim 153°$ regional dust storm strongly affected temperatures at Jezero. The first effect was a warming of the near-surface atmosphere with peak temperatures increased by 12 K and a progressive decrease of surface temperatures during a period of 4 sols. The coldest maximum surface temperature was observed with a phase lag of 3 sols with respect to the maximum atmospheric temperatures, indicating changes in the vertical dust distribution. Comparing temperature data with other studies of this dust storm from Perseverance data (Lemmon et al., 2022; Vicente-Retortillo et al., 2022), we interpret the cooling of the surface and the warming of air temperatures as evidence of low altitude dust controlling atmospheric temperatures on the arrival of the storm.

- Near surface air temperatures measured by MEDA and previous missions that operated at tropical latitudes have a similar seasonal trend. Temperature differences are small when MEDA temperatures are compared with MPF and increase when compared with VL1, with mean air temperatures at Jezero being ∼6.5 K warmer than at the VL1 landing site over the same seasonal period. This is most likely a consequence of the different albedos of those locations, with Jezero's albedo being smaller than that at the VL1 landing site.

- A comparison of MEDA temperatures at Jezero with prelanding model predictions offers reasonably good agreement. The deviations between the various models and MEDA data show a dependence on the different model considerations of surface properties (thermal inertia and albedo) and optical depths. Future modeling of the near surface atmosphere at Jezero will improve by addressing the heterogeneous properties of the surface found over the MEDA investigation.

Future MEDA measurements of temperatures covering a full Martian year, and with further variations of surface properties and atmospheric optical depths, will improve our knowledge of atmospheric processes in the ASL at Jezero. The fast response time of the sensors, and the rich variation of thermal gradients and fluctuations, will offer an excellent data set to understand convective and other turbulent processes in the Martian PBL.

Appendix A: Thermal Contamination Effects on ATS Raw Data

The main artifacts that appear in ATS raw data occur when environmental winds are not able to efficiently couple the sensors with the atmosphere, leaving an individual or several ATS inside the thermal boundary layer of the rover. The main thermal contamination effects that appear in the data are shown in Figure A1a and largely depend on the rover orientation and sensor locations indicated in Figure A1b. These thermal contamination effects are as follows:

- *Thermal pulses from the RTG*: This effect is typically observed at night and can produce temperature excesses of +10 K with winds of about 3 ms^{-1}. These type of effects are predicted in numerical simulations of warm RTG plumes and their interaction with the rover and its mast (Gómez-Elvira et al., 2012; Lorenz & Sotzen, 2014), with specific CFD simulations for M2020 similar to those shown in Figure S2 in Supporting Information S1 confirming the numbers above. Red arrows in Figure A1a highlight some of these events. An example of an extremely long event lasting half an hour is shown in Figure S3 in Supporting Information S1.
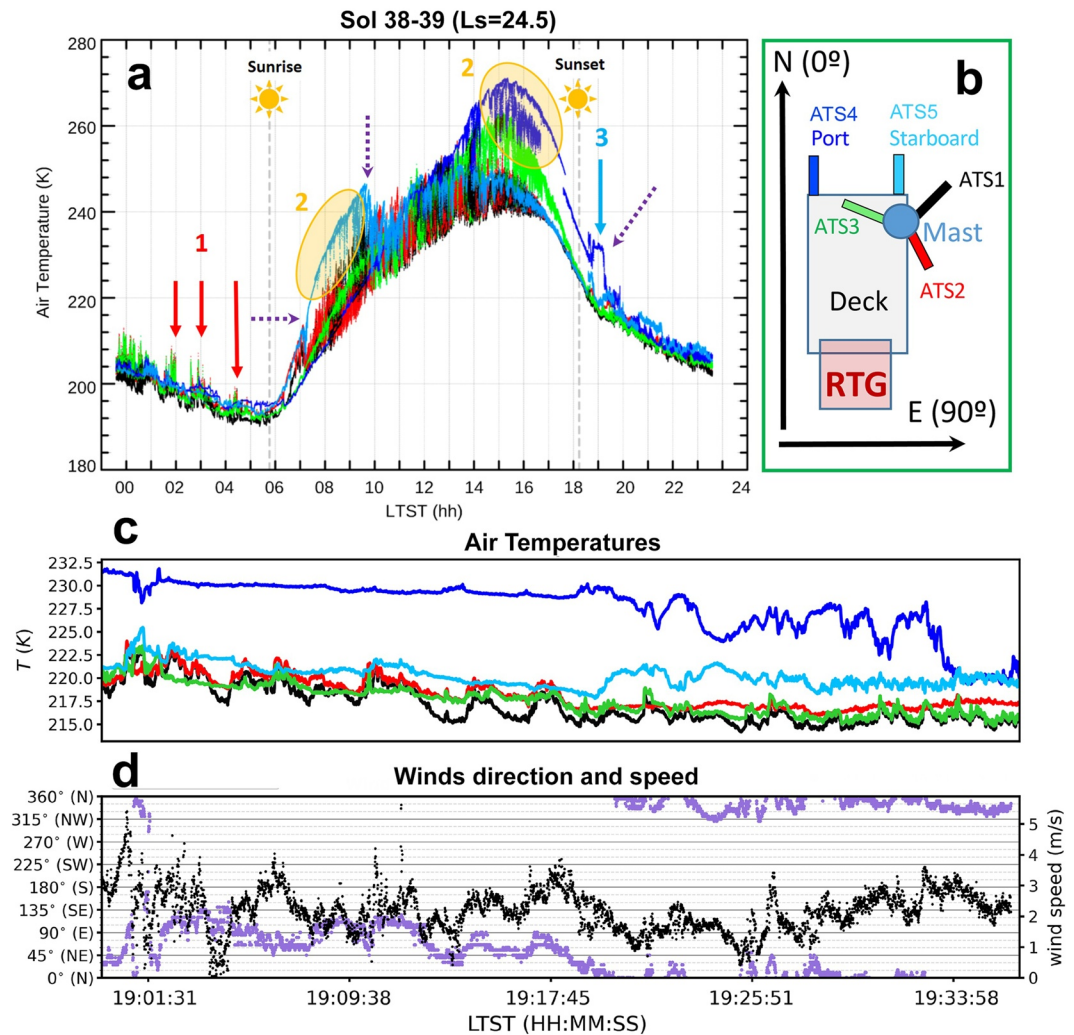
Figure A1. Air Temperature Sensors (ATS) data on the five sensors over two sols: (a) Raw ATS temperature data combining two consecutive sols. Colors used for each ATS follow the color convention defined in (b). Arrows and numbers mark thermal contamination events described in the text. (b) Sketch showing the orientation of the rover to the North on the sols the data was acquired and the relative position of the five ATS and the Radioisotope Thermoelectric Generator. (c) Structure of a sudden drop in temperatures measured by ATS4. (d) Wind intensity (right-axis, black points) and direction where the wind comes from (left-axis, purple points). Data in panels c and d correspond to sol 42 that shared an orientation identical to the one on sols 38–39, when winds were not available.

Daytime convection and higher temperatures mask or largely reduce these effects. Note that the RTG does not influence the measurements in ATS4 and ATS5, which are sheltered on the front of the rover as observed in CFD simulations of M2020. This effect is mitigated by choosing the ATS sensor in the RSM with the lower temperature. Events of contamination from the RTG generally affect short time intervals during the night and are not removed or filtered-out in the analysis presented in this paper because of their low impact on the overall temperature results.

- *Solar illumination of surfaces near individual ATS*: The warming/cooling of rover surfaces at a different rate than the atmosphere produces a thermal boundary layer around the rover, especially at sunrise/sunset. This effect is sensed differently in each ATS depending on the solar illumination of the surrounding surfaces and the winds, which are able to couple the sensors with the atmosphere (Figure S2 in Supporting Information S1) and hence very dependent on the orientation of the rover. Local heating occurs near the sensors that are exposed to the sun while shielded from environmental winds. This effect is generally stronger in ATS4 and ATS5 because of their placement on the rover body. Yellow circles in Figure A1a highlight this effect. This thermal contamination is easily removed by choosing the ATS at each altitude with the lower temperature.

- *Overheated surfaces of the rover sheltered from environmental winds*: This is a typical defect in ATS4, which is shielded behind Perseverance's robotic arm. This is manifested by high temperatures with nearly no fluctuations. A blue arrow in Figure A1a highlights an example. This can also affect an individual ATS in the wake of the RSM producing higher temperatures than the other two ATS at the RSM, typically occurring at night.

All the sources of artificial thermal contamination depend on the geometric orientation of the rover (Figure A1b) with respect to the environmental winds. Overheated sensors affected by these effects can sometimes show an abrupt drop in temperature when winds change in direction. These effects are highlighted with dotted purple arrows in Figure A1a. An example is shown in higher detail in Figure A1c with a comparison with simultaneous winds in Figure A1d.

ATS4-5 at 0.84 m are generally sheltered from the environmental winds in most directions, since the mechanical structure of the rover acts as an obstacle to the wind (Bardera et al., 2018). Frontal side winds can cool efficiently one of the ATS on the front of the rover but the range of favorable wind directions is limited. For instance, in Figures A1c and A1d, with the rover pointing to the North, winds coming directly from the North are not efficient in cooling ATS4, whereas winds slightly skewed coming from the North-West perform better on coupling this sensor with the environment. The combination of daytime warm temperatures and intense winds seems to be strong enough to diminish the thermal contamination of ATS4-5 during daytime hours.

These panels also show that measurements in ATS1-3 are not affected by the intensity of the winds, which vary from 1 to 5 ms^{-1}. These velocities are enough to produce a good coupling of the ATS in the RSM with the environment (see Figure S2 in Supporting Information S1). A practical example is shown in Figures A1c and A1d, where ATS1 is the sensor that is most closely located upwind from the RSM, resulting in the coldest temperature measurements. When two sensors are upwind (ATS1 and ATS2 at 19:00-19:10 LTST), both measure equivalent temperatures. The sensor located in the wake of the winds interacting with the RSM measures warmer temperatures and the least temperature fluctuations. For example, winds from the east make ATS3 temperatures warmer than those of ATS1 and ATS2 at 19:00–19:10 LTST. Conversely, when the winds change to blow from the North-West, ATS2 becomes the sensor located in the wake of the RSM, which results in warmer temperature recordings with less temperature fluctuations in this sensor.

Appendix B: ATS Data Selection

A reasonable assumption to retrieve a single atmospheric temperature at each ATS altitude (0.84 and 1.45 m) is that the minimum temperature at each altitude and time is the closest value to the environmental temperature. In most cases, sources of thermal contamination are intense enough to clearly show the sensor that is performing better (see Figures A1c and A1d). However, selecting the sensor that has the minimum temperature at each time has a drawback in the artificial reduction of thermal fluctuations that is produced when two sensors have temperatures that cross each other in the time series.

We use an algorithm that tracks the minimum temperature switching from one sensor to another smoothly and preserving temperature fluctuations. For each time step and altitude, we calculate a contribution factor to the air temperature that is 1 for the ATS with the minimum temperature and 0 for all others. Then, we smooth the time
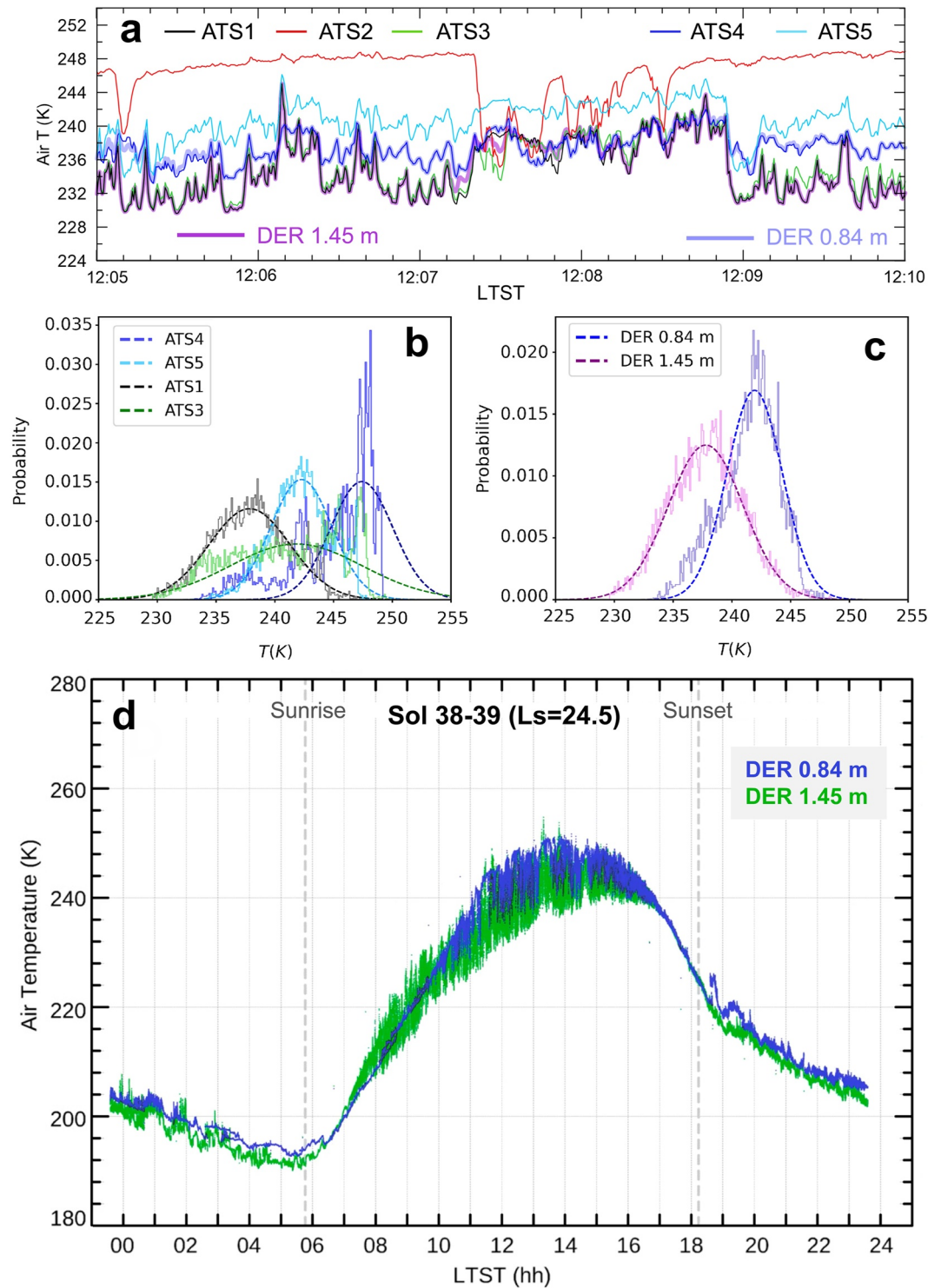
Figure B1. (a) A typical time series of the five Air Temperature Sensors (ATS) around noon on sol 35. Individual colors are equivalent to those in Figure A1. Thick blue line and thick violet line show the selected temperatures at 0.84 and 1.45 m, respectively. (b) Histograms of the ATS 1, 3, 4, and 5 and the corresponding Gaussian fits extended over a block of data of 1 hour at noon. The probability distributions of the sensors that are less exposed to the environment (ATS 3 and 4) are far from a Gaussian distribution. (c) Histograms of the derived temperatures at 0.84 m (blue) and at 1.45 m (violet) resemble a Gaussian distribution with a cold tail at 0.84 m. (d) Derived temperatures at 0.84 m (blue) and 1.45 m (green) for the diurnal data shown in Figure A1a.

series of contribution factors with a time window of 1 minute obtaining smoothly varying contribution factors for each ATS. The air temperature is a weighted average of the various ATS measurements using their respective contribution factors.

An example of this procedure is shown in Figure B1. Panel a show the ATS temperatures during 5 min and their fluctuations. Derived temperatures are shown with thick lines and lie around the lower temperature measurement while preserving its fluctuations. Panels b and c show the statistical distribution of temperatures in each sensor and those of the derived values. Based on similar arguments to those in Tillman (1972), the cold tail of the derived temperatures at 0.84 m in panel c is related to the lower reliability at this level than at 1.45 m. Finally, the derived clean temperatures at 0.84 and 1.45 m for the example shown in Appendix A is shown in panel d.

The software to read ATS raw data and obtain derived single temperatures at 0.84 and 1.45 m is available in Hueso et al. (2022).

Data Availability Statement

The MEDA data used in this study are available via the NASA Planetary Data System (PDS) (de la Torre Juarez & Rodriguez-Manfredi, 2021). Derived MEDA ATS temperatures at 0.84 and 1.45 m and the program to derive these data from RAW MEDA ATS data are available in Hueso et al. (2022). Albedo and thermal inertia values from MEDA data are available in Martínez et al. (2023). Atmospheric opacities at Jezero are calculated from publicly available data from the ZCAM instrument via the PDS (Bell & Maki, 2021). Reduced meteorological data from Viking Lander 1 (J. Tillman, 1989) and Mars Pathfinder (Murphy, 1998) are publicly available via the PDS. The Mars Climate Database (MCD) is accessible at http://www-mars.lmd.jussieu.fr/mcd_python/.

References

Banfield, D., Conrath, B., Pearl, J. C., Smith, M. D., & Christensen, P. (2000). Thermal tides and stationary waves on Mars as revealed by Mars Global Surveyor thermal emission spectrometer. *Journal of Geophysical Research*, 105(E4), 9521–9538. https://doi.org/10.1029/1999JE001161

Banfield, D., Rodriguez-Manfredi, J. A., Russell, C., Rowe, K., Leneman, D., Lai, H., et al. (2019). Insight auxiliary payload sensor suite (APSS). *Space Science Reviews*, 215(1), 1–33. https://doi.org/10.1007/s11214-018-0570-x

Banfield, D., Spiga, A., Newman, C. E., Forget, F., Lemmon, M. T., Lorenz, R. D., et al. (2020). The atmosphere of Mars as observed by InSight. *Nature Geoscience*, 13(3), 190–198. https://doi.org/10.1038/s41561-020-0534-0

Bardera, R., Sor, S., Garcia-Magariño, A., Gómez-Elvira, J., Marin, M., Navarro, S., et al. (2018). Experimental and numerical characterization of the flow around the Mars 2020 rover. *Journal of Spacecraft and Rockets*, 55(5), 1136–1143. https://doi.org/10.2514/1.a34217

Barnes, J. R. (1980). Time spectral analysis of midlatitude disturbances in the Martian atmosphere. *Journal of the Atmospheric Sciences*, 37(9), 2002–2015. https://doi.org/10.1175/1520-0469(1980)037<2002:tsaomd>2.0.co;2

Barnes, J. R., Haberle, R. M., Wilson, R. J., Lewis, S. R., Murphy, J. R., & Read, P. L. (2017). The global circulation. In R. M. Haberle, R. T. Clancy, F. Forget, M. D. Smith, & R. W. Zurek (Eds.), *The atmosphere and climate of Mars* (pp. 229–294). Cambridge University Press. https://doi.org/10.1017/9781139060172.009

Battalio, J. M., Martínez, G. M., Newman, C. E., de la Torre Juarez, M., Sánchez-Lavega, A., & Víudez-Moreiras, D. (2022). Planetary waves traveling between Mars Science Laboratory and Mars 2020. *Geophysical Research Letters*, 49(21). https://doi.org/10.1029/2022gl100866

Bell, J. F., & Maki, J. N. (2021). Mars 2020 mast camera zoom bundle, from Arizona state University mastcam-z instrument team, calibrated products. *NASA Planetary Data System*. https://doi.org/10.17189/Q3TS-C749

Bell, J. F., Maki, J. N., Alwmark, S., Ehlmann, B. L., Fagents, S. A., Grotzinger, J. P., et al. (2022). Geological, multispectral, and meteorological imaging results from the Mars 2020 perseverance rover in Jezero crater. *Science Advances*, 8(47), eabo4856. https://doi.org/10.1126/sciadv.abo4856

Charney, J. G. (1990). The dynamics of long waves in a baroclinic westerly current. In R. S. Lidzen, E. N. Lorenz, & G. W. Platzman (Eds.), *The atmosphere—A challenge*. American Meteorological Society, Boston, Ma. https://doi.org/10.1007/978-1-944970-35-2_13

Chide, B., Bertrand, T., Lorenz, R. D., Munguira, A., Hueso, R., Sánchez-Lavega, A., et al. (2022). Acoustics reveals short-term air temperature fluctuations near Mars' surface. *Geophysical Research Letters*, 49(21), e2022GL100333. https://doi.org/10.1029/2022GL100333

Christensen, P. R. (1988). Global albedo variations on Mars: Implications for active aeolian transport, deposition, and erosion. *Journal of Geophysical Research*, 93(B7), 7611–7624. https://doi.org/10.1029/JB093iB07p07611

Davy, R., Davis, J. A., Taylor, P. A., Lange, C. F., Weng, W., Whiteway, J., & Gunnlaugson, H. P. (2010). Initial analysis of air temperature and related data from the phoenix met station and their use in estimating turbulent heat fluxes. *Journal of Geophysical Research*, 115(E3), E00E13. https://doi.org/10.1029/2009je003444

de la Torre Juarez, M., & Rodriguez-Manfredi, J. A. (2021). Mars 2020 MEDA bundle. *NASA Planetary Data System*. https://doi.org/10.17189/1522849

Fergason, R. L., Christensen, P. R., & Kieffer, H. H. (2006). High-resolution thermal inertia derived from the thermal emission imaging system (THEMIS): Thermal model and applications. *Journal of Geophysical Research (Planets)*, 111(E12), E12004. https://doi.org/10.1029/2006JE002735

Foken, T. (2008). Micrometeorology. https://doi.org/10.1007/978-3-540-74666-9_1

Gómez-Elvira, J., Armiens, C., Carrasco, I., Genzer, M., Gómez, F., Haberle, R., et al. (2014). Curiosity's rover environmental monitoring station: Overview of the first 100 sols. *Journal of Geophysical Research: Planets*, 119(7), 1680–1688. https://doi.org/10.1002/2013JE004576

Gómez-Elvira, J., Armiens, C., Castañer, L., Domínguez, M., Genzer, M., Gómez, F., et al. (2012). REMS: The environmental sensor suite for the Mars Science Laboratory rover. *Space Science Reviews*, 170(1–4), 583–640. https://doi.org/10.1007/s11214-012-9921-1

Guzewich, S. D., de la Torre Juárez, M., Newman, C. E., Mason, E., Smith, M. D., Miller, N., et al. (2021). Gravity wave observations by the Mars Science Laboratory REMS pressure sensor and comparison with mesoscale atmospheric modeling with MarsWRF. *Journal of Geophysical Research: Planets*, *126*(8), e06907. https://doi.org/10.1029/2021JE006907

Guzewich, S. D., Lemmon, M., Smith, C., Martínez, G., de Vicente-Retortillo, Á., Newman, C., et al. (2019). Mars Science Laboratory observations of the 2018/Mars year 34 global dust storm. *Geophysical Research Letters*, *46*(1), 71–79. https://doi.org/10.1029/2018gl080839

Guzewich, S. D., Newman, C. E., de la Torre Juárez, M., Wilson, R. J., Lemmon, M., Smith, M. D., et al. (2016). Atmospheric tides in Gale crater, Mars. *Icarus*, *268*, 37–49. https://doi.org/10.1016/j.icarus.2015.12.028

Haberle, R. M., de la Torre Juárez, M., Kahre, M. A., Kass, D. M., Barnes, J. R., Hollingsworth, J. L., et al. (2018). Detection of northern hemisphere transient eddies at gale crater Mars. *Icarus*, *307*, 150–160. https://doi.org/10.1016/j.icarus.2018.02.013

Hamilton, V. E., Vasavada, A. R., Sebastián, E., de la Torre Juárez, M., Ramos, M., Armiens, C., et al. (2014). Observations and preliminary science results from the first 100 sols of MSL rover environmental monitoring station ground temperature sensor measurements at gale crater. *Journal of Geophysical Research: Planets*, *119*(4), 745–770. https://doi.org/10.1002/2013je004520

Hess, S. L., Henry, R. M., Leovy, C. B., Ryan, J. A., & Tillman, J. E. (1977). Meteorological results from the surface of Mars: Viking 1 and 2. *Journal of Geophysical Research*, *82*(B28), 4559–4574. https://doi.org/10.1029/JS082i028p04559

Hueso, R., Munguira, A., Sánchez-Lavega, A., De la Torre-Juárez, M., Rodríguez-Manfredi, J., & Lepinette, A. (2022). Derived environmental temperatures at Jezero crater from air temperature sensors' measurements on the perseverance rover. [Dataset]. Zenodo. https://doi.org/10.5281/zenodo.7461835

Hueso, R., Newman, C. E., del Río-Gaztelurrutia, T., Munguira, A., Sánchez-Lavega, A., Toledo, D., et al. (2023). Convective vortices and dust devils detected and characterized by Mars 2020. *Journal of Geophysical Research: Planets*, *128*, e2022JE007516. https://doi.org/10.1029/2022JE007516

James, P. B., Christensen, P. R., Clancy, R. T., Lemmon, M. T., & Withers, P. (2017). History of Mars Atmosphere Observations. In R. M. Haberle, R. T. Clancy, F. Forget, M. D. Smith, & R. W. Zurek (Eds.), *The Atmosphere and Climate of Mars (Cambridge Planetary Science)* (pp. 20–41). Cambridge: Cambridge University Press. https://doi.org/10.1017/9781139060172.003

Kieffer, H. H., Martin, T. Z., Peterfreund, A. R., Jakosky, B. M., Miner, E. D., & Palluconi, F. D. (1977). Thermal and albedo mapping of Mars during the Viking primary mission. *Journal of Geophysical Research*, *82*(B28), 4249–4292. https://doi.org/10.1029/JS082i028p04249

Larsen, S. E., Jørgensen, H. E., Landberg, L., & Tillman, J. (2002). Aspects of the atmospheric surface layers on Mars and Earth. *Boundary-Layer Meteorology*, *105*(3), 451–470. https://doi.org/10.1023/a:1020338016753

Lemmon, M. T., Smith, M. D., Viudez-Moreiras, D., de la Torre-Juarez, M., Vicente-Retortillo, A., Munguira, A., et al. (2022). Dust, sand, and winds within an active Martian storm in Jezero crater. *Geophysical Research Letters*, *49*(17), e2022GL100126. https://doi.org/10.1029/2022GL100126

Leovy, C. B. (1977). The atmosphere of Mars. *Scientific American*, *237*(1), 34–43. https://doi.org/10.1038/scientificamerican0777-34

Lewis, S. R., Collins, M., Read, P. L., Forget, F., Hourdin, F., Fournier, R., et al. (1999). A climate database for Mars. *Journal of Geophysical Research*, *104*(E10), 24177–24194. https://doi.org/10.1029/1999je001024

Lorenz, R. D., & Sotzen, K. S. (2014). Buoyant thermal plumes from planetary landers and rovers: Application to sizing of meteorological masts. *Planetary and Space Science*, *90*, 81–89. https://doi.org/10.1016/j.pss.2013.10.011

Martínez, G. M., Newman, C. E., De Vicente-Retortillo, A., Fischer, E., Renno, N., Richardson, M., et al. (2017). The modern near-surface Martian climate: A review of in-situ meteorological data from Viking to curiosity. *Space Science Reviews*, *212*(1), 295–338. https://doi.org/10.1007/s11214-017-0360-x

Martínez, G. M., Sebastián, E., Vicente-Retortillo, A., Smith, M. D., Johnson, J. R., Fischer, E., et al. (2023). Surface energy budget, albedo and thermal inertia at Jezero crater, Mars, as observed from the Mars 2020 MEDA instrument. *Journal of Geophysical Research: Planets*, *128*, e2022JE007537. https://doi.org/10.1029/2022JE007537

Martínez, G. M., Valero, F., & Vázquez, L. (2009). Characterization of the Martian convective boundary layer. *Journal of the Atmospheric Sciences*, *66*(7), 2044–2058. https://doi.org/10.1175/2009jas3007.1

Mason, E. L., & Smith, M. D. (2021). Temperature fluctuations and boundary layer turbulence as seen by Mars exploration rovers miniature thermal emission spectrometer. *Icarus*, *360*, 114350. https://doi.org/10.1016/j.icarus.2021.114350

Maurice, S., Chide, B., Murdoch, N., Lorenz, R. D., Mimoun, D., Wiens, R. C., et al. (2022). In situ recording of Mars soundscape. *Nature*, *605*(7911), 653–658. https://doi.org/10.1038/s41586-022-04679-0

Maurice, S., Wiens, R. C., Bernardi, P., Caïs, P., Robinson, S., Nelson, T., et al. (2021). The SuperCam instrument suite on the Mars 2020 rover: Science objectives and Mast-unit description. *Space Science Reviews*, *217*(3), 47. https://doi.org/10.1007/s11214-021-00807-w

Miller, N., de la Torre Juárez, M., & Tamppari, L. (2018). The effect of bagnold dunes slopes on the short timescale air temperature fluctuations at gale crater on Mars. *Geophysical Research Letters*, *45*(21), 11588–11594. https://doi.org/10.1029/2018GL080542

Millour, E., Forget, F., & Lewis, S. (2017). Mars climate database v. 5.3. User manual. ESTEC Contract. Retrieved from http://www-mars.lmd.jussieu.fr/mars/info_web/user_manual_5.3.pdf

Murphy, J. (1998). *MPFL-M-ASIMET-3-RDR-SURF-V1.0*. NASA Planetary Data System. https://doi.org/10.17189/nshg-bx61

Newman, C. E., de la Torre Juárez, M., Pla-García, J., Wilson, R. J., Lewis, S. R., Neary, L., et al. (2021). Multi-model Meteorological and aeolian predictions for Mars 2020 and the Jezero crater region. *Space Science Reviews*, *217*(1), 20. https://doi.org/10.1007/s11214-020-00788-2

Newman, C. E., Hueso, R., Lemmon, M. T., Munguira, A., Vicente-Retortillo, Á., Apestigue, V., et al. (2022). The dynamic atmospheric and aeolian environment of Jezero Crater, Mars. *Science Advances*, *8*(21), eabn3783. https://doi.org/10.1126/sciadv.abn3783

Ordonez-Etxeberria, I., Hueso, R., Sánchez-Lavega, A., & Vicente-Retortillo, Á. (2020). Characterization of a local dust storm on Mars with REMS/MSL measurements and MARCI/MRO images. *Icarus*, *338*, 113521. https://doi.org/10.1016/j.icarus.2019.113521

Perez-Grande, I., Peinado, L., Chamorro, A., Torralbo, I., Alonso, G., Rodriguez Manfredi, J. A., et al. (2017). Thermal design of the air temperature sensor (ATS) and the thermal InfraRed sensor (TIRS) of the Mars environmental dynamics analyzer (MEDA) for Mars 2020. In *47th international conference on environmental systems*.

Pérez-Izquierdo, J., Sebastián, E., Martínez, G. M., Bravo, A., Ramos, M., & Manfredi, J. A. R. (2018). The thermal infrared sensor (TIRS) of the Mars environmental dynamics analyzer (MEDA) instrument onboard Mars 2020, a general description and performance analysis. *Measurement*, *122*, 432–442. https://doi.org/10.1016/j.measurement.2017.12.004

Petrosyan, A., Galperin, B., Larsen, S. E., Lewis, S. R., Määttänen, A., Read, P. L., et al. (2011). The Martian atmospheric boundary layer. *Reviews of Geophysics*, *49*(3), RG3005. https://doi.org/10.1029/2010RG000351

Pla-García, J., Rafkin, S. C. R., Martinez, G. M., Vicente-Retortillo, Á., Newman, C. E., Savijärvi, H., et al. (2020). Meteorological predictions for Mars 2020 perseverance rover landing site at Jezero crater. *Space Science Reviews*, *216*(8), 148. https://doi.org/10.1007/s11214-020-00763-x

Pollack, J. B., Colburn, D., Kahn, R., Hunter, J., Van Camp, W., Carlston, C., & Wolf, M. (1977). Properties of aerosols in the Martian atmosphere, as inferred from Viking lander imaging data. *Journal of Geophysical Research*, *82*(28), 4479–4496. https://doi.org/10.1029/js082i028p04479

Pollack, J. B., Colburn, D. S., Flasar, F. M., Kahn, R., Carlston, C., & Pidek, D. (1979). Properties and effects of dust particles suspended in the Martian atmosphere. *Journal of Geophysical Research*, *84*(B6), 2929–2945. https://doi.org/10.1029/jb084ib06p02929

Rafkin, S. C. R., Spiga, A., & Michaels, T. I. (2017). Mesoscale meteorology. In R. M. Haberle, R. T. Clancy, F. Forget, M. D. Smith, & R. W. Zurek (Eds.), *The atmosphere and climate of mars* (pp. 203–228). Cambridge University Press. https://doi.org/10.1017/9781139060172.008

Read, P. L., Galperin, B., Larsen, S. E., Lewis, S. R., Määttänen, A., Petrosyan, A., et al. (2017). The Martian Planetary Boundary Layer. In In Haberle, R. M., Clancy, R. T., Forget, F., Smith, M. D. & Zurek, R. W. (Eds.), The Atmosphere and Climate of Mars (Cambridge Planetary Science, pp. 172–202). Cambridge: Cambridge University Press. https://doi.org/10.1017/9781139060172.007

Rodriguez-Manfredi, J., de la Torre Juárez, M., Alonso, A., Apéstigue, V., Arruego, I., Atienza, T., et al. (2021). The Mars environmental dynamics analyzer, meda. a suite of environmental sensors for the Mars 2020 mission. *Space Science Reviews*, *217*(3), 1–86. https://doi.org/10.1007/s11214-021-00816-9

Rodriguez-Manfredi, J., Gomez-Gomez, F., Gomez-Elvira, J., Navarro, S., Prieto-Ballesteros, O., Sebastian, E., et al. (2017). Atmospheric science with the Mars 2020 rover-the MEDA instrument. In *6th Mars Atmosphere modeling and observations*.

Rodríguez-Manfredi, J. A., de la Torre Juárez, M., Sánchez-Lavega, A., Hueso, R., Martinez, G. M., Lemmon, M. T., et al. (2023). The diverse meteorology of jezero crater over the first 250 sols of perseverance on Mars. *Nature Geoscience*, *16*, 19–28. https://doi.org/10.1038/s41561-022-01084-0

Ryan, J., & Henry, R. (1979). Mars atmospheric phenomena during major dust storms, as measured at surface. *Journal of Geophysical Research*, *84*(B6), 2821–2829. https://doi.org/10.1029/jb084ib06p02821

Sánchez-Lavega, A., del Rio-Gaztelurrutia, T., Hueso, R., de la Torre Juárez, M., Martínez, G. M., Harri, A. M., et al. (2023). Mars 2020 perseverance rover studies of the Martian atmosphere over Jezero from pressure measurements. *Journal of Geophysical Research: Planets*, *128*, e2022JE007480. https://doi.org/10.1029/2022JE007480

Savijärvi, H. I., Martinez, G. M., & Harri, A. M. (2022). Surface energy fluxes and temperatures at jezero crater, Mars. *Journal of Geophysical Research: Planets*, *127*, e2022JE007438. https://doi.org/10.1029/2022JE007438

Schofield, J., Barnes, J. R., Crisp, D., Haberle, R. M., Larsen, S., Magalhaes, J., et al. (1997). The Mars pathfinder atmospheric structure investigation/meteorology (ASI/MET) experiment. *Science*, *278*(5344), 1752–1758. https://doi.org/10.1126/science.278.5344.1752

Sebastián, E., Martínez, G. M., Ramos, M., Haenschke, F., Ferrándiz, R., Fernández, M., & Manfredi, J. A. R. (2020). Radiometric and angular calibration tests for the MEDA-TIRS radiometer onboard NASA's Mars 2020 mission. *Measurement*, *164*, 107968. https://doi.org/10.1016/j.measurement.2020.107968

Sebastián, E., Martínez, G. M., Ramos, M., Perez-Grande, I., Sobrado, J., & Manfredi, J. A. R. (2021). Thermal calibration of the MEDA-TIRS radiometer onboard NASA's perseverance rover. *Acta Astronautica*, *182*, 144–159. https://doi.org/10.1016/j.actaastro.2021.02.006

Smith, M. D., Bougher, S. W., Encrenaz, T., Forget, F., & Kleinböhl, A. (2017). Thermal structure and composition. In R. M. Haberle, R. T. Clancy, F. Forget, M. D. Smith, & R. W. Zurek (Eds.), *Asteroids, comets, meteors - acm2017* (pp. 20–41). https://doi.org/10.1017/9781139060172.004

Smith, M. D., Wolff, M. J., Lemmon, M. T., Spanovich, N., Banfield, D., Budney, C. J., et al. (2004). First atmospheric science results from the Mars exploration rovers mini-tes. *Science*, *306*(5702), 1750–1753. https://doi.org/10.1126/science.1104257

Smith, M. D., Wolff, M. J., Spanovich, N., Ghosh, A., Banfield, D., Christensen, P. R., et al. (2006). One Martian year of atmospheric observations using MER Mini-Tes. *Journal of Geophysical Research*, *111*(E12), E12S13. https://doi.org/10.1029/2006je002770

Spanovich, N., Smith, M. D., Smith, P. H., Wolff, M. J., Christensen, P. R., & Squyres, S. W. (2006). Surface and near-surface atmospheric temperatures for the Mars Exploration Rover landing sites. *Icarus*, *180*(2), 314–320. https://doi.org/10.1016/j.icarus.2005.09.014

Streeter, P. M., Lewis, S. R., Patel, M. R., Holmes, J. A., & Kass, D. M. (2019). Surface warming during the 2018/Mars year 34 global dust storm. *Geophysical Research Letters*, *47*(9), e2019GL083936. https://doi.org/10.1029/2019GL083936

Stull, R. B. (1988). An introduction to boundary layer meteorology. https://doi.org/10.1007/978-94-009-3027-8

Sutton, J. L., Leovy, C. B., & Tillman, J. E. (1978). Diurnal variations of the Martian surface layer meteorological parameters during the first 45 sols at two Viking lander sites. *Journal of the Atmospheric Sciences*, *35*(12), 2346–2355. https://doi.org/10.1175/1520-0469(1978)035<2346:dvotms>2.0.co;2

Tillman, J. (1972). The indirect determination of stability, heat and momentum fluxes in the atmospheric boundary layer from simple scalar variables during dry unstable conditions. *Journal of Applied Meteorology and Climatology*, *11*(5), 783–792. https://doi.org/10.1175/1520-0450(1972)011<0783:tidosh>2.0.co;2

Tillman, J. (1989). *VL1/VL2-M-MET-4-BINNED-P-T-V-V1.0*. NASA Planetary Data System. https://doi.org/10.17189/1518948

Tillman, J. E., Landberg, L., & Larsen, S. E. (1994). The boundary layer of Mars: Fluxes, stability, turbulent spectra, and growth of the mixed layer. *Journal of the Atmospheric Sciences*, *51*(12), 1709–1727. https://doi.org/10.1175/1520-0469(1994)051<1709:tblomf>2.0.co;2

Vicente-Retortillo, A., Martínez, G. M., Lemmon, M. T., Hueso, R., Sullivan, R., Newman, C. E., et al. (2022). Changes in Surface Albedo Induced by Dust Devils and the MY 36 Ls=155° Dust Storm at Jezero Crater. In *Seventh International Workshop on the Mars Atmosphere: Modelling and Observations* (p. 1512).

Vicente-Retortillo, Á., Valero, F., Vázquez, L., & Martínez, G. M. (2015). A model to calculate solar radiation fluxes on the Martian surface. *Journal of Space Weather and Space Climate*, *5*, A33. https://doi.org/10.1051/swsc/2015035

Viúdez-Moreiras, D., de la Torre-Juarez, M. d. l., Gómez-Elvira, J., Lorenz, R. D., Apéstigue, V., Guzewich, S., et al. (2022). Winds at the Mars 2020 landing site. Part 2: Wind variability and turbulence. *Journal of Geophysical Research: Planets*, *127*(12), e2022JE007523. https://doi.org/10.1029/2022JE007523

Viúdez-Moreiras, D., Lemmon, M., Newman, C. E., Guzewich, S., Mischna, M., Gómez-Elvira, J., et al. (2022). Winds at the Mars 2020 landing site: Part 1. Near-Surface wind patterns at Jezero crater. *Journal of Geophysical Research: Planets*, *127*(12), e2022JE007522. https://doi.org/10.1029/2022JE007522

Viúdez-Moreiras, D., Newman, C., De la Torre, M., Martínez, G., Guzewich, S., Lemmon, M., et al. (2019). Effects of the my34/2018 global dust storm as measured by msl rems in gale crater. *Journal of Geophysical Research: Planets*, *124*(7), 1899–1912. https://doi.org/10.1029/2019je005985

Viúdez-Moreiras, D., Newman, C., Forget, F., Lemmon, M., Banfield, D., Spiga, A., et al. (2020). Effects of a large dust storm in the near-surface atmosphere as measured by insight in Elysium Planitia, Mars. Comparison with contemporaneous measurements by Mars Science Laboratory. *Journal of Geophysical Research: Planets*, *125*(9), e2020JE006493. https://doi.org/10.1029/2020JE006493